Geophys. J. Int. (2007) **169,** 1009–1027 doi: 10.1111/j.1365-246X.2006.03312.x

Post-seismic motion following the 1997 Manyi (Tibet) earthquake: InSAR observations and modelling

Isabelle Ryder,[1] Barry Parsons,[1] Tim J. Wright[1] and Gareth J. Funning[2]

[1] *COMET, Department of Earth Sciences, University of Oxford, UK. E-mail: isabelle@earth.ox.ac.uk*
[2] *Berkeley Seismological Laboratory, California, USA*

Accepted 2006 November 23. Received 2006 November 23; in original form 2006 June 2

SUMMARY

On November 8 1997 a M_w 7.6 earthquake occurred in the Manyi region of northern Tibet, near the western end of the Kunlun Fault. Over 7 m of left-lateral slip occurred on a 200-km-long fault. Here we use InSAR observations of post-seismic surface deformation following the Manyi earthquake to investigate possible causal mechanisms. Time-series of deformation are constructed from 26 interferograms, covering the entire length of the fault for nearly 4 yr after the earthquake. Three different modelling approaches are used to try and understand the observed variations in surface displacement. First order poroelastic models predict displacement fields which do not match those observed. Modelling of viscoelastic stress relaxation in a half-space with standard linear solid rheology beneath an elastic lid provides a reasonable fit to the observations, and demonstrates that two relaxation times are needed to characterize the post-seismic transient. The best-fitting viscosity is 4×10^{18} Pa s, and the fully-relaxed shear modulus is 32 per cent of the purely elastic value. A model with a Maxwell viscoelastic half-space underlying the lid cannot explain the observations: at later times, larger viscosities are required than at earlier times. This increase in effective viscosity with time may be consistent with stress relaxation occurring in a power-law rheology. The time-series are also inverted for distributed afterslip on an extension of the coseismic rupture. Along-strike correlation of coseismic and post-seismic slip maxima suggests that afterslip is a plausible mechanism. The maximum slip in the afterslip model is 0.72 m after 3 yr, and the equivalent moment release is approximately 20 per cent of the coseismic moment. This study shows that it is possible to rule out certain mechanisms as the dominant post-seismic process, but with the current InSAR data set it is difficult to distinguish between other plausible options.

Key words: afterslip, crustal deformation, InSAR, post-seismic motion, Tibet, viscoelastic relaxation.

1 INTRODUCTION

Post-seismic motion has been observed by satellite geodesy following several large strike-slip earthquakes since the early 1990s, including Landers in 1992 (e.g. Massonnet *et al.* 1994, 1996; Peltzer *et al.* 1996), Hector Mine in 1999 (e.g. Pollitz *et al.* 2001; Jacobs *et al.* 2002), Izmit in 1999 (e.g. Bürgmann et al. 2002; Ergintav *et al.* 2002; Hearn *et al.* 2002) and Denali in 2002 (Pollitz 2005). It is recognized that this motion is a response to the redistribution of stresses brought about by an earthquake, that is, the motion records stress relaxation somewhere in the upper part of the lithosphere. However, exactly where and how the stresses are relaxed remains an open question. Various mechanisms have been proposed and investigated: afterslip on a discrete plane (e.g. Bürgmann *et al.* 2002), creep in a viscous or viscoelastic shear zone (e.g. Hearn *et al.* 2002), viscoelastic relaxation in the lower crust/upper mantle (e.g. Pollitz *et al.* 2000), and poroelastic rebound (e.g. Jónsson *et al.* 2003). Results from different authors suggest that no single mechanism applies to all case studies. Furthermore, more than one process may occur in any individual case study. Essential to determining which mechanism is most plausible are 2-D time-series of surface deformation. Different mechanisms can produce spatially similar displacement fields (Savage 1990; Hearn 2003). Temporal and spatial behaviour together are more useful in diagnosing what is happening at depth. By pursuing this type of study, we aim to understand the rheological properties beneath the seismogenic layer, as well as learning how stresses are relaxed following an earthquake.

The M_w 7.6 Manyi earthquake occurred on November 8 1997, in a remote region of the northern Tibetan plateau (Fig. 1). The left-lateral strike-slip fault, which lies ∼200 km west of the Kunlun Fault, broke the surface and is mappable from satellite imagery. Peltzer *et al.* (1999) estimate a maximum surface offset of 7 m, and Funning *et al.* (2006) estimate 7.6 m, with slip occurring down to a depth of 20 km. The asymmetry of the observed displacement field is

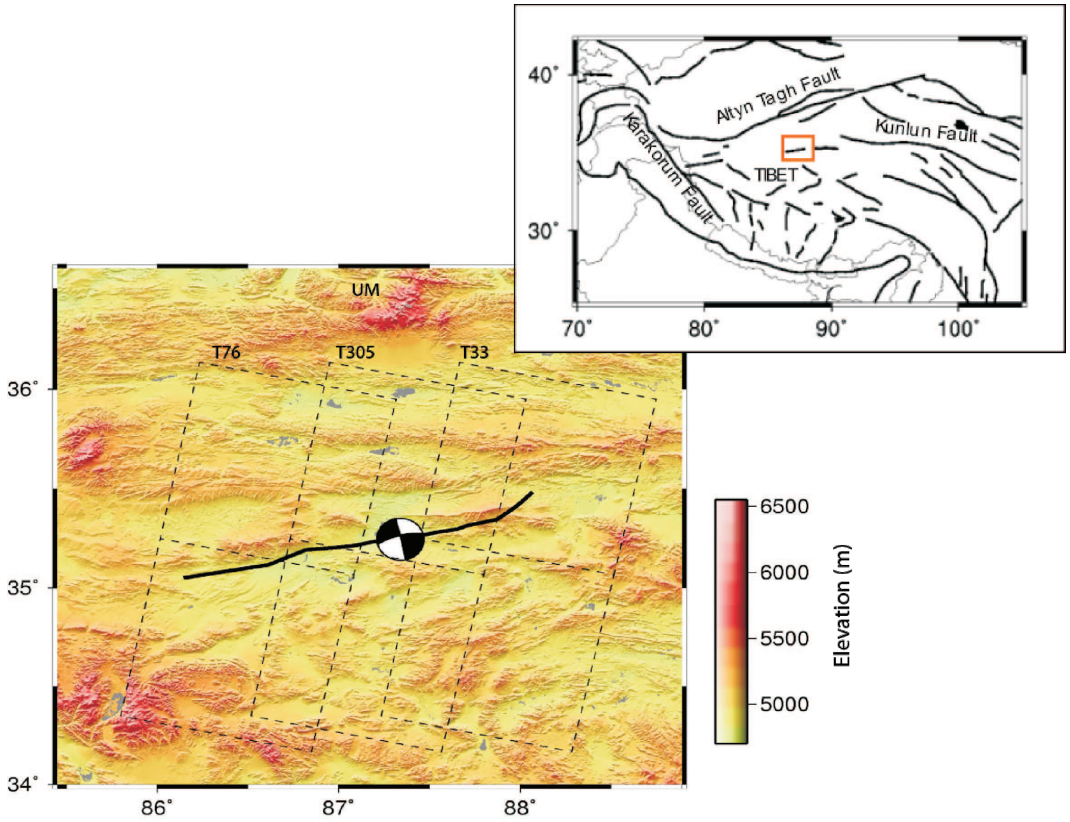

Figure 1. Location map (inset) and shaded relief topography for the Manyi area. DEM is 90 m SRTM. Fault trace is shown in black and fault plane solution is taken from the Harvard catalogue. T76, T305 and T33 refer to SAR tracks 76, 305 and 33, marked by black dotted lines. UM denotes the Ulugh Muztagh mountain.

explained by Peltzer *et al.* (1999) as being due to a difference in tensile and compressive elastic moduli, but Funning *et al.* (2006) reproduce the asymmetry by a change in fault dip from southward in the west to northward in the east (Table 3). The present study uses post-seismic Interferometric Synthetic Aperture Radar (InSAR) data as a basis for investigating stress relaxation in the first few years following the earthquake. The aim is to understand what mechanism is responsible for the observed post-seismic surface deformation, and to determine the rheological structure of the upper lithosphere.

2 AFTERSHOCKS

Relative to other large earthquakes, the number of aftershocks following the Manyi earthquake died away slowly with time. If the number of aftershocks $n(t)$ at time t after the earthquake is plotted against time for the first 5 months, a curve can be fitted (Fig. 2) using the modified Omori law:

$$n(t) = k(t + c)^{-p}, \quad (1)$$

where k, c and p are constants. The exponent p is a measure of the decay rate of aftershocks. For the Manyi earthquake, $p = 0.4$. This is lower than the p values that are typically computed for large earthquakes (e.g. Kisslinger & Jones 1991; Shcherbakov *et al.* 2004). This earthquake is also unusual in having only relatively small aftershocks, all of the aftershocks being more than two orders of magnitude smaller than the main shock (Velasco *et al.* 2000). The total moment contributed by the aftershocks in the first 5 months following the main shock is 1.44×10^{18} N m, less than 1 per cent of the coseismic moment release. As a result, very little surface deformation related to aftershocks will have been observed at the surface, even though the decay rate is slow. We choose, therefore, not to consider aftershocks for the remainder of this study, other than discussing the implications of their time-dependent behaviour and small moment release.

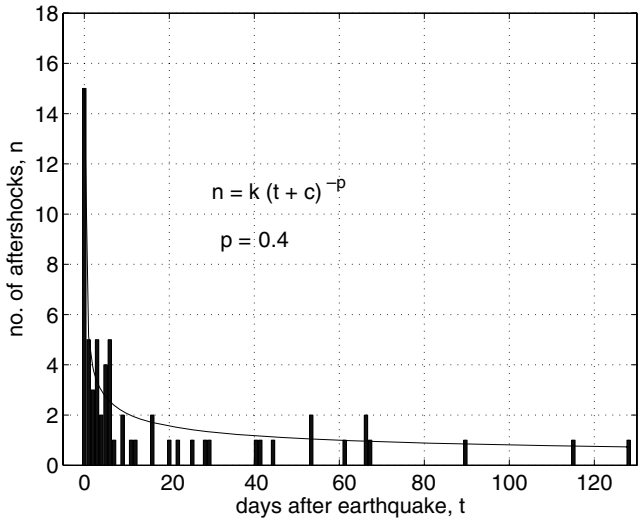

Figure 2. Number of aftershocks as a function of time after the Manyi earthquake. Aftershock dates are taken from the International Seismological Centre. A curve with the functional form of the modified Omori law is fitted. The exponent p is 0.4.

Table 1. Details of the 26 interferograms used in this study. Dates are in day-month-year format. For reference, the earthquake occurred on 1997 November 8. Perpendicular baseline is given in the final column. All interferograms consist of two frames (2889 and 2907). Data is © European Space Agency.

Number	Track	Start date	End date	Start orbit	End orbit	Baseline (m)
1	76	16-11-1997	21-12-1997	13 457	13 958	43
2	76	16-11-1997	04-07-1999	13 457	21 974	271
3	76	21-12-1997	04-07-1999	13 958	21 974	314
4	76	25-01-1998	25-04-1999	14 459	20 972	57
5	76	25-01-1998	04-07-1999	14 495	21 974	106
6	305	02-12-1997	04-08-1998	13 686	17 193	69
7	305	02-12-1997	08-09-1998	13 686	17 694	157
8	305	02-12-1997	02-11-1999	13 686	23 706	30
9	305	06-01-1998	04-08-1998	14 187	17 193	44
10	305	06-01-1998	08-09-1998	14 187	17 694	44
11	305	06-01-1998	02-11-1999	14 187	23 706	143
12	305	10-02-1998	17-03-1998	14 688	15 189	262
13	305	10-02-1998	26-12-2000	14 688	29 718	32
14	305	17-03-1998	04-08-1998	15 189	17 193	124
15	305	21-04-1998	04-08-1998	15 690	17 193	85
16	305	21-04-1998	08-09-1998	15 690	17 694	173
17	305	04-08-1998	08-09-1998	17 193	17 694	88
18	305	04-08-1998	02-11-1999	13 915	20 428	99
19	33	18-12-1997	18-03-1999	13 915	20 428	254
20	33	18-12-1997	01-07-1999	13 915	21 913	240
21	33	18-12-1997	23-12-1999	13 915	24 436	26
22	33	26-02-1998	07-12-2000	14 416	29 446	24
23	33	07-05-1998	27-05-1999	15 919	21 430	18
24	33	01-07-1999	23-12-1999	21 913	24 436	266
25	33	01-07-1999	13-09-2001	21 913	33 454	217
26	33	23-12-1999	13-09-2001	24 436	33 454	49

3 INTERFEROGRAMS

SAR data were obtained from the European Remote Sensing satellite, ERS-2, on multiple dates following the earthquake. The acquisitions cover almost 4 yr, with the earliest being eight days after the earthquake. From these acquisitions, 51 post-seismic interferograms were constructed, using the Repeat Orbit Interferometry Package (ROI_PAC) processing software developed at Caltech/JPL (Rosen *et al.* 2004). Three descending SAR tracks were used, covering the entire length of the fault. Each interferogram uses two SAR frames (2889 and 2907), and so covers an area on the ground of ∼120 km (cross track) by ∼210 km (along track). Some interferograms were also constructed using four frames (2871, 2889, 2907 and 2925) for the central track. A 90 m digital elevation model (DEM) produced from NASA's Shuttle Radar Topography Mission (Farr & Kobrick 2000; Rodriguez *et al.* 2006) was used to remove topographic fringes. Particularly noisy or incoherent interferograms were discarded, leaving a set of 26 good interferograms (see Table 1 and Fig. 3). The smallest and largest perpendicular baselines of this final set are 18 and 314 m, respectively. These translate into altitudes of ambiguity of 523 and 30 m. The altitude of ambiguity is the change in altitude, or in the present context, height error in the DEM, required to give one fringe in a wrapped interferogram. The quoted vertical accuracy of the SRTM DEM is <7 m (Rodriguez *et al.* 2006), so DEM errors will at worst result in one quarter of a fringe, or 7 mm of range change. Out of the 26 interferograms, 17 have perpendicular baselines less than 150 m (altitude of ambiguity greater than 63 m). Two interferograms from each track are shown in Fig. 4. One of these interferograms is shown at larger scale in Fig. 5. A measure of atmospheric noise is given by the standard deviation in range change of non-deforming regions; averaged over all interferograms, this standard deviation is 0.5 cm. The excellent

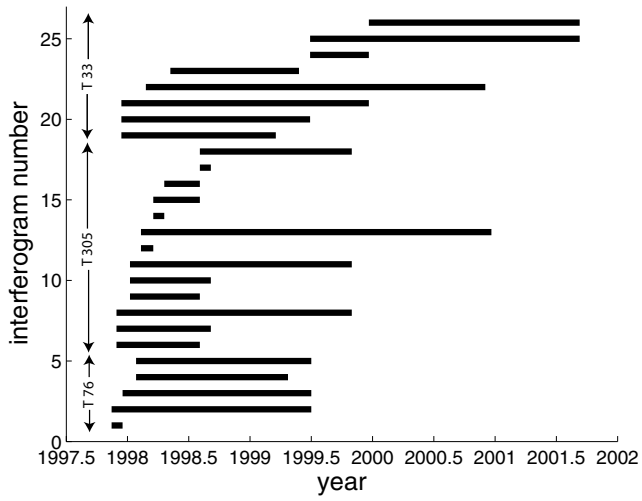

Figure 3. Time intervals covered by the 26 post-seismic interferograms. T76, T305 and T33 are track numbers.

coherence and low atmospheric noise level of the interferograms collectively are consistent with previous InSAR studies of the Tibetan plateau (e.g. Wright *et al.* 2004), and are likely due to the lack of vegetation and the arid climate at the high elevation (∼5 km) of this part of the plateau.

To minimize errors in the displacement field due to insufficient or incorrect orbital information, corrections are implemented which remove any orbital signal as far as possible. Since earthquake-related displacements must decrease to zero at a finite distance from the fault, a correction is applied which brings the far-field deformation

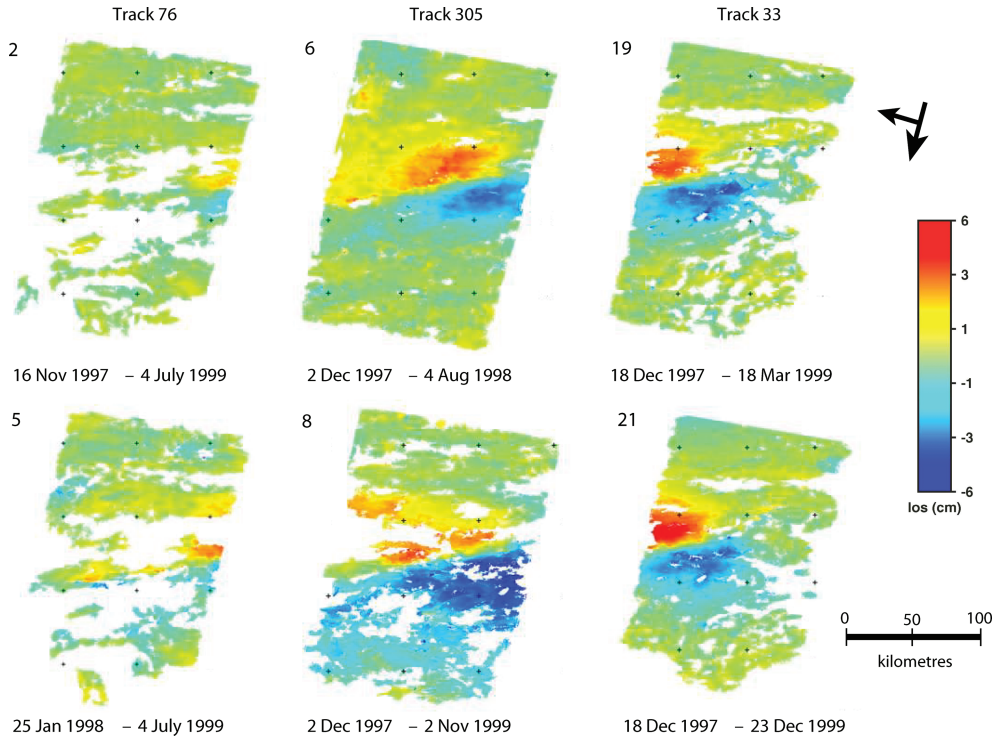

Figure 4. Post-seismic interferograms. Two interferograms for each of the three tracks are shown. Numbers refer to those in Table 1. Positive range change is line-of-sight displacement away from the satellite. Positive range change (red) occurs north of the fault and negative range change (blue) south of the fault. Arrows show direction of descending satellite track (SSW) and look direction (WNW).

as close to zero as possible. Post-processing linear and quadratic corrections are made by masking out the deforming regions from the interferograms, finding the plane or quadratic surface that best fits the non-deforming regions, and subtracting this trend from the entire interferogram. Quadratic corrections bring the far-field signal closest to zero. We perform this correction on two- and four-frame interferograms for the central track. The four-frame interferograms have larger non-deforming areas than those with two frames, and so would be expected to give a more robust correction. The standard deviation of the difference between the two- and four-frame interferograms whose profiles are shown in Fig. 5 is 0.31 cm, which is less than the level of noise in the interferograms: the standard deviation of the undeforming areas averaged over all two-frame interferograms for track 305 is 0.54 cm. We therefore, use two-frame interferograms in the succeeding analysis.

Lobes of positive and negative range change can be seen in the north and south parts of the interferograms, respectively, (Figs 4 and 5a). We display the interferograms using the range change convention that positive displacements are line-of-sight displacements away from the satellite. The location of the boundary between the two lobes agrees with the fault trace as mapped from satellite imagery (Peltzer *et al.* 1999; Funning *et al.* 2006). Profiles across the centre of the fault (e.g. Fig. 5b) show maximum displacement at about 10–20 km from the fault, with an amplitude on the order of a few centimetres in the line-of-sight. The maximum peak-to-trough range change is 10.4 cm in an interferogram that covers from 1 month to 2 yr after the earthquake (interferogram no. 8). The lack of GPS measurements in this remote area, coupled with the lack of ascending InSAR data, makes it impossible to resolve horizontal and vertical components of motion, but if all the motion were horizontal and strike-parallel, this peak line-of-sight deformation would correspond to ∼30 cm of left-lateral offset.

4 CONSTRUCTION OF TIME-SERIES

We constructed three separate time-series, one for each track. The data lend themselves well to spatial interpolation owing to a smoothly varying signal and excellent coherence. Spline interpolation (Wessel & Smith 1998) in the spatial domain is applied to each interferogram individually. Removal of data gaps in this way means that all pixels can be considered in the construction of the time-series. Next, the images are down-sampled by a factor of about 10. For each pixel, the line-of-sight displacement relative to a reference time is calculated using a least-squares approach modified from Schmidt & Bürgmann (1998) and Berardino *et al.* (2002).

Let **t** be a vector of SAR acquisition dates in chronological order. For a dataset containing N interferograms constructed from S acquisitions on different dates, the range change $r_{t_a t_b}$ between times t_a, the start time, and t_b, the end time, for a given interferogram can be written as

$$r_{t_a t_b} = \sum_{k=a}^{b-1} v_{k,k+1}(t_{k+1} - t_k). \tag{2}$$

Here, $v_{k,k+1}$ is the velocity between the kth and $(k+1)^{th}$ time. Let **p** and **q** be index vectors of size N for the interferogram start and end dates, respectively. These index vectors record the ordinal number of the start/end dates (i.e. the dates in **t**) of all the interferograms, with each component referring to one interferogram. We can generalize (2) into a matrix equation for the entire set of interferograms:

$$\mathbf{Tv} = \mathbf{r}. \tag{3}$$

In (3), **v** is a vector (of size $S-1$) of successive velocities, [$v_{0,1}$, $v_{1,2}$, ..., $v_{S-2,S-1}$], **r** is a vector of interferogram displacements, and the $N \times (S-1)$ matrix **T** references time intervals. The jm^{th}

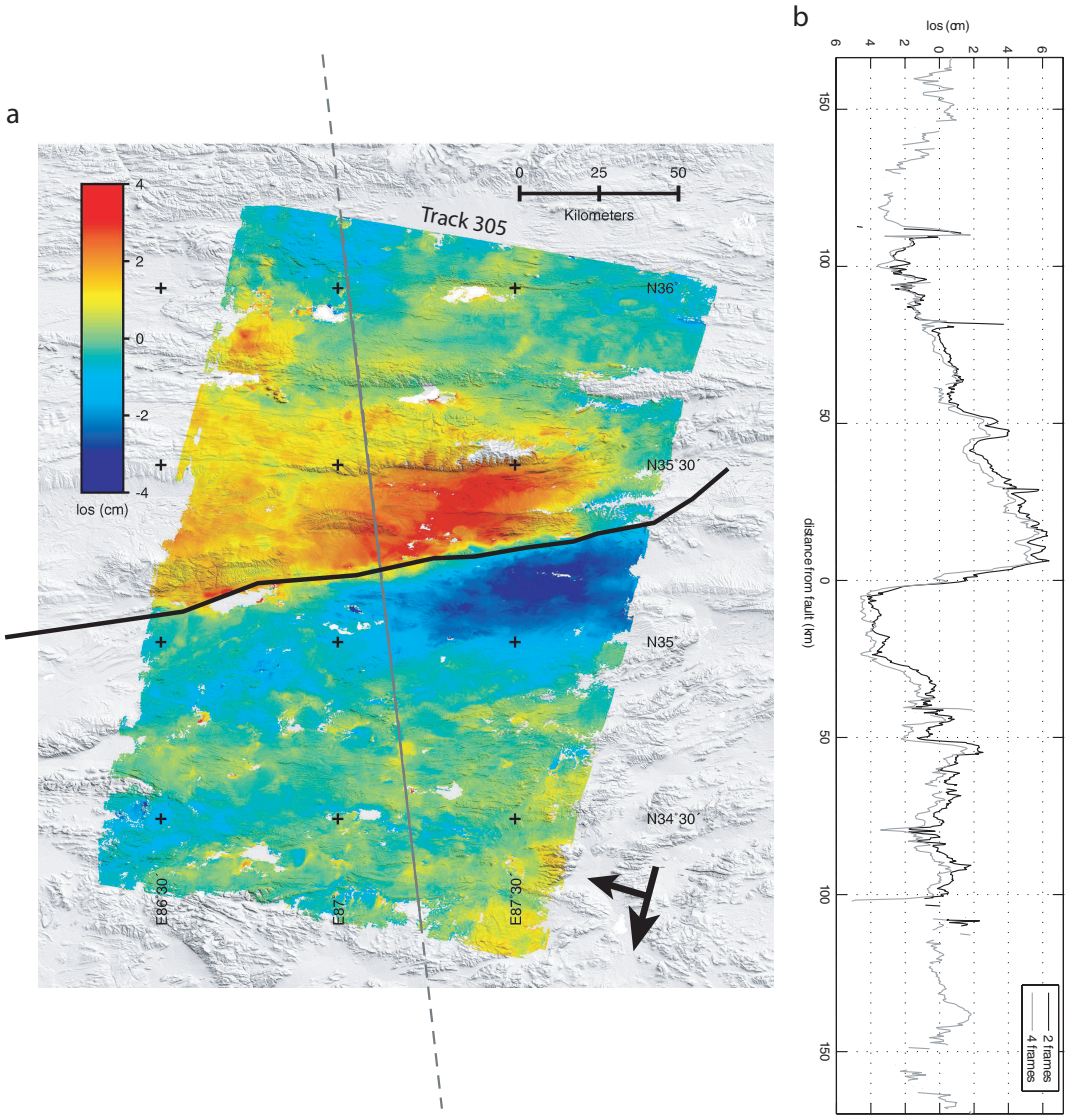

Figure 5. (a) Post-seismic interferogram overlaid on shaded relief SRTM topography. Interferogram start date is 2 December 1997 and end date is August 4 1998. Colour scale is range change in cm. Black line shows 11-segment coseismic fault trace as mapped from satellite imagery (Funning *et al.* 2006). Arrows show direction of descending satellite track (SSW) and look direction (WNW). Grey line shows location of two- and four-frame profiles shown in b. (b) Profiles through centre of fault for two- and four-frame interferograms, both with a quadratic post-processing correction applied.

element of $\mathbf{T}$ is given by

$$T_{jm} = t_{m+1} - t_m \tag{4}$$

for the non-zero elements ($p_j + 1 \leq m \leq q_j$). We perform the inversion using velocities rather than displacements to avoid large discontinuities in the solution (Berardino *et al.* 2002).

Temporal smoothing is applied to reduce the effects of atmospheric noise on the time-series for each pixel. A constant velocity constraint would be written as

$$v_{k,k+1} = v_{k-1,k} \tag{5}$$

for $2 \leq k \leq (S-1)$. In matrix form, this constraint is

$$\mathbf{T^s v} = \mathbf{0}, \tag{6}$$

where $\mathbf{0}$ is an $(S-2)$ column vector of zeros, and the non-zero elements of the $(S-2)$ by $(S-1)$ matrix $\mathbf{T}^s$ are given by

$$T^s_{j,j} = -1 \tag{7}$$

$$T^s_{j,j+1} = +1 \tag{8}$$

for $1 \leq j \leq (S-2)$. (6) can be weighted by some factor γ in the final matrix equation, such that the temporal decay curve is smoothed without being completely straightened:

$$\begin{bmatrix} \mathbf{T} \\ \gamma \mathbf{T^s} \end{bmatrix} [\mathbf{v}] = \begin{bmatrix} \mathbf{r} \\ \mathbf{0} \end{bmatrix}. \tag{9}$$

The temporal smoothing factor γ is chosen by taking the point of maximum curvature of a misfit versus roughness curve for different smoothing factors (Fig. 6). This smoothing reduces anomalous atmospheric signals in single interferograms. Spatial smoothing between adjacent pixels is not applied. Once a least-squares solution for the velocities is found, the velocities are integrated over time to give the displacements at successive dates. Finally, the initial velocity is extended back to the time of the earthquake itself, on the assumption that the initial post-seismic transient is linear for the first month or so. Examination of displacement–time curves for

Table 2. Dates of the time-series for each of the three SAR tracks. For reference, dates are given in day-month-year format, decimal year format and as number of days since the earthquake.

Track	Image number	Date (dd-mm-yyyy)	Year (decimal)	Number of days
76	1	16-11-1997	1997.87	9
(west)	2	21-12-1997	1997.96	44
	3	25-02-1998	1998.07	110
	4	25-04-1999	1999.31	169
	5	04-07-1999	1999.50	604
305	1	02-12-1997	1997.91	25
(centre)	2	06-01-1998	1998.02	60
	3	10-02-1998	1998.11	95
	4	17-03-1998	1998.21	130
	5	21-04-1998	1998.30	165
	6	04-08-1998	1998.59	270
	7	08-09-1998	1998.68	305
	8	02-11-1999	1999.83	725
	9	26-12-2000	2000.97	1145
33	1	18-12-1997	1997.95	41
(east)	2	26-02-1998	1998.15	111
	3	07-05-1998	1998.35	181
	4	18-03-1999	1999.21	496
	5	27-05-1999	1999.40	566
	6	01-07-1999	1999.49	601
	7	23-12-1999	1999.97	776
	8	12-07-2000	2000.92	978

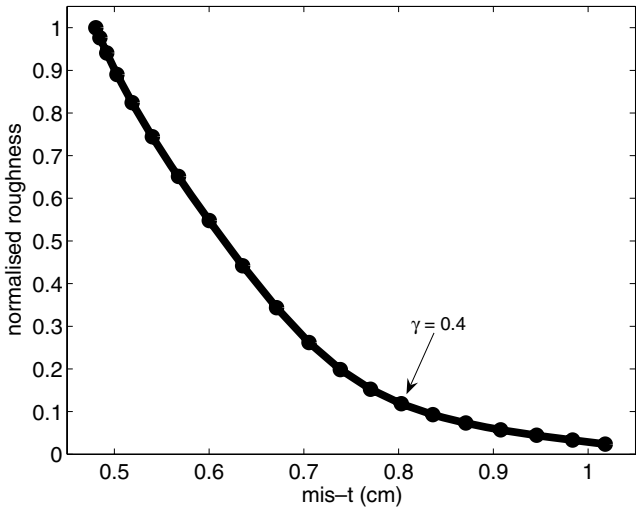

Figure 6. Roughness plotted against misfit for different smoothing factors in the time-series matrix (9). The point of maximum curvature marks the optimal smoothing factor (γ) of 0.4.

individual points on the ground (Fig. 9) suggests that linear interpolation in this way is a reasonable approximation.

The time-series for each of the three tracks has its own unique set of dates, given for reference in Table 2. For viscoelastic modelling purposes, these original time-series with their unique dates are retained, but for ease of visual comparison the time-series shown in Fig. 7 involve some temporal interpolation. The reference date for all three time-series is the earthquake itself, and the time-series for the eastern and western tracks have been interpolated temporally to bring the dates into line with those of the central track. A general trend that is observed in all three time-series is an increase in the magnitude of deformation over time. This increase is charted in the profile plots of Fig. 8. It should be noted that there is significant overlap between the western and central tracks, and between the central and eastern tracks, as for the interferograms themselves (see Fig. 1). The line-of-sight displacement field is asymmetrical across the fault, with surface motion on the south side of the fault shifted to the east with respect to motion north of the fault. Range change decay curves are shown for two pixels, one north of the fault and one south of the fault, in Fig. 9. To gain a first order idea of the rate of decay of surface displacement, absolute range change is summed over all pixels and an exponential curve is fitted. The curve has the form $A(1 - e^{-t/\tau})$, where A and τ are constants and t is time, though no physical significance is attached to the exponential functionality. The decay time is 0.7 yr. This is also the modal decay time when similar curve-fitting is performed for individual points on the ground.

5 MODELLING

The three following subsections each pursue a quantitative investigation of a particular post-seismic deformation mechanism. The three models—poroelastic rebound, viscoelastic stress relaxation and afterslip—are treated separately for modelling purposes, though it is acknowledged that more than one mechanism may occur at any one time. We wish to know whether any one of the mechanisms on its own can explain the post-seismic surface motion observed by InSAR. For the modelling, only the deforming parts of the time-series images (i.e. about 70 km either side of the fault) are used.

5.1 Poroelastic modelling

Stress changes associated with an earthquake rupture can induce pore pressure gradients in surrounding rock. Flow of fluid between

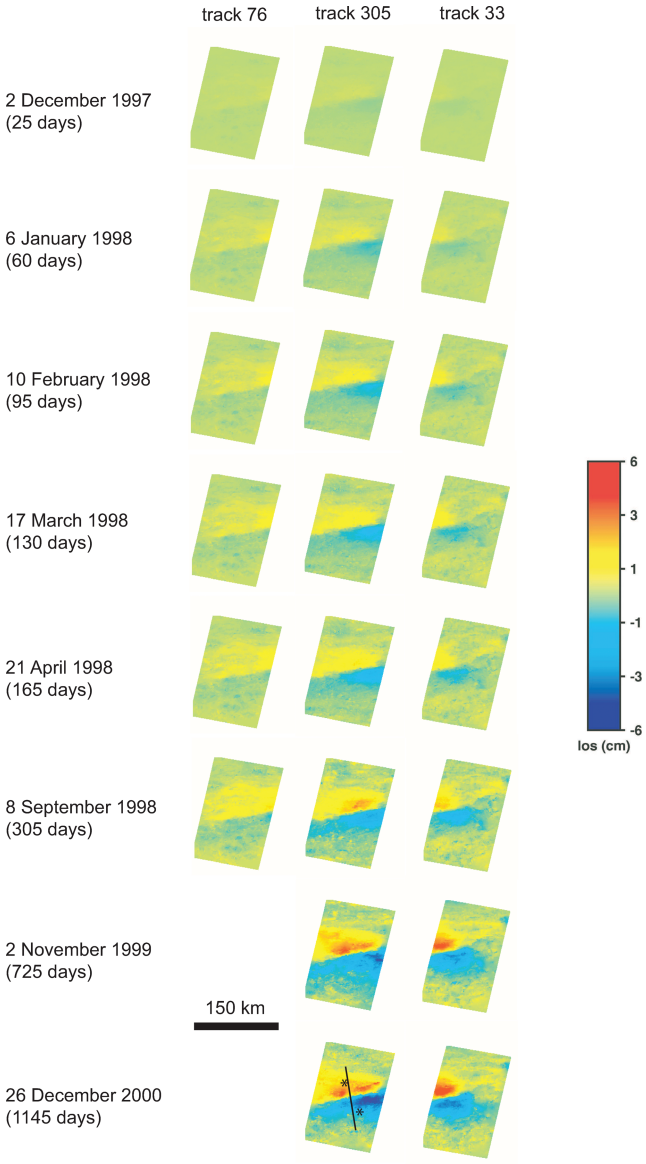

Figure 7. Post-seismic time-series. Line in bottom centre image marks location of profiles in Fig. 8, and stars denote locations of time-series curves shown in Fig. 9.

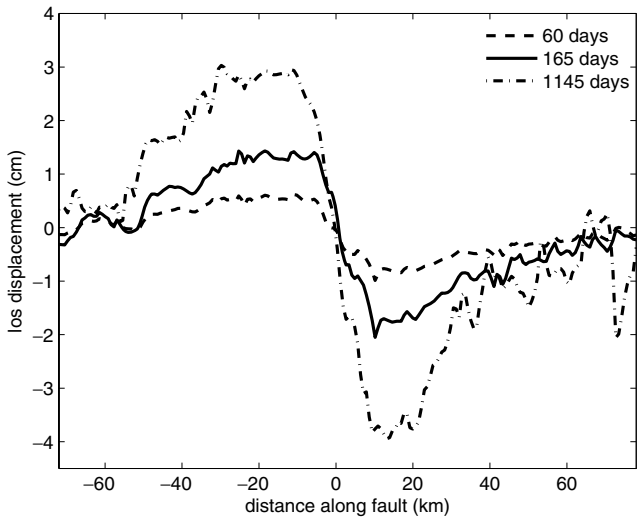

Figure 8. Strike-perpendicular profiles of line-of-sight displacement through the centre of the fault, at different times after the earthquake. Profiles are taken from the central time-series shown in Fig. 7.

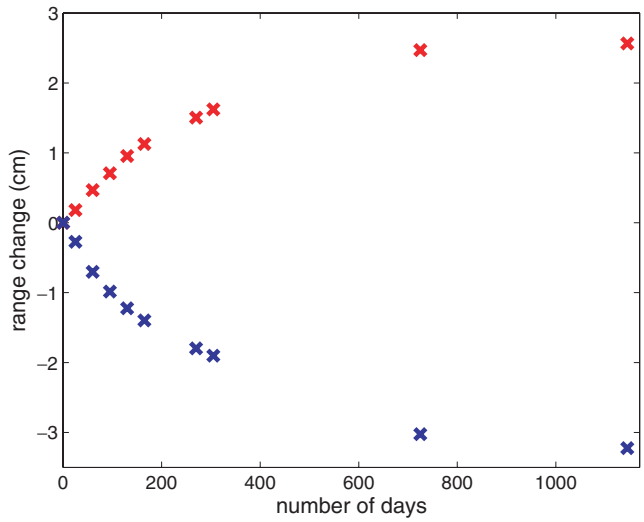

Figure 9. Range change decay curves for two pixels, one north of the fault (red) and one south of the fault (blue). Locations are marked by stars in Fig. 7.

pores gradually relaxes these gradients, so that hydrostatic equilibrium is regained. This fluid flow deforms the medium and causes motion at the surface. In this analysis we treat the crust as poroelastic, that is, as an elastic matrix saturated with water in its pores. The transient behaviour can be approximated by a temporary increase in the Poisson's ratio, representing the initial change in pore fluid pressure (Rice & Cleary 1976), which decays back to the pre-earthquake equilibrium value over a finite time (Peltzer *et al.* 1996). Hence the surface motion resulting from pore fluid flow can been estimated from the difference between the coseismic displacement fields calculated using different Poisson's ratios (Peltzer *et al.* 1996; Jónsson *et al.* 2003; Fialko 2004b). Values of Poisson's ratio used are 0.24 and 0.21: the equilibrium value of 0.24 is that used by Funning *et al.* (2006) for the Manyi coseismic inversions, and the difference in Poisson's ratio is typically 0.03 (Peltzer *et al.* 1996). We use the slip distribution obtained by Funning *et al.* (2006) in modelling the coseismic surface deformation. The line-of-sight displacement field predicted by complete poroelastic rebound is shown in Fig. 10. The amplitude varies in proportion to the difference in Poisson's ratio. Although the curves in Fig. 9 imply that post-seismic motion might not be complete by the final date of the time-series, it is reasonable to assume that the spatial pattern of the deformation field will not change significantly beyond this date and only the magnitude of deformation will change. The striking spatial mismatch between the pattern of deformation throughout the time-series and the first order poroelastic prediction indicates that the dominant physical mechanism is not likely to be poroelastic rebound. It is possible that pore fluid flow may contribute in a minor way to the surface signal, but we do not explore this possibility here.

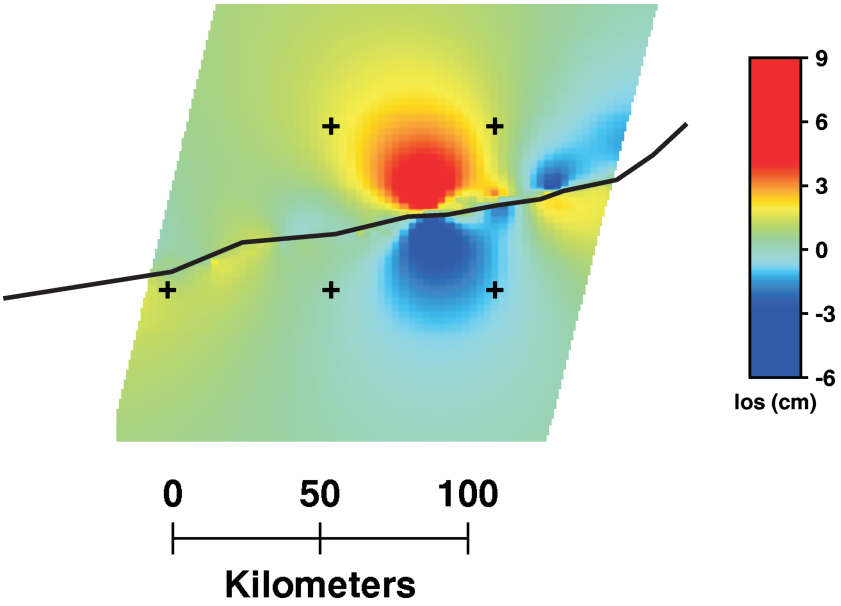

Figure 10. Range change predicted by poroelastic rebound model, for the central track (track 305). The spatial deformation pattern bears little similarity to that of the time-series (Fig. 7). Black line marks position of fault.

Table 3. Earthquake source parameters as obtained by Funning *et al.* (2006) from inversion of InSAR data. Segment numbers refer to those in Fig. 15. Lon and Lat give the longitude and latitude at the centre of the top of each fault segment. *L* in column 4 is length and *D* in column 5 refers to the maximum depth of the fault segment.

Segment number	Lon	Lat	*L* (km)	*D* (km)	Strike	Dip	Rake	Slip (m)
1	86.380	35.084	43.1	11.7	80	85	2.6	1.72
2	86.715	35.154	20.3	11.7	66	85	2.6	2.01
3	86.943	35.201	23.3	11.7	85	85	2.6	3.39
4	87.177	35.231	19.9	11.7	77	85	2.6	5.49
5	87.350	35.255	12.0	14.2	266	85	−9.3	5.39
6	87.482	35.270	12.5	14.2	258	85	−9.3	4.80
7	87.604	35.290	10.1	14.2	259	85	−9.3	3.63
8	87.680	35.306	4.3	14.2	247	85	−9.3	3.17
9	87.787	35.329	16.0	14.2	256	85	−9.3	2.94
10	87.925	35.378	11.8	14.2	233	85	−9.3	1.16
11	88.023	35.447	11.6	14.2	225	85	−9.3	0

5.2 Viscoelastic modelling

5.2.1 Method

Any earthquake-induced stress changes occurring within viscoelastic material in the crust or upper mantle will potentially be relaxed by viscous flow, with the time constant of stress relaxation governed by the viscosity. Any linear viscoelastic system has a stress relaxation response $\sigma(t)$ (constant strain) and a creep relaxation response $\varepsilon(t)$ (constant stress). The time constants in the expressions for $\sigma(t)$ and $\varepsilon(t)$ describe the temporal behaviour of the system, and are functions of rigidity and viscosity. A particular rheology may have one or more associated time constants. Following an earthquake, both strain and stress vary continually as stress relaxation occurs, so neither $\sigma(t)$ nor $\varepsilon(t)$ are directly applicable. The temporal decay of strain rate is, however, still characterized by the material time constants.

In this study, we consider two linear viscoelastic rheologies: Maxwell and standard linear solid. Element representations of these rheologies are shown in Fig. 11. A Maxwell body has an elastic element with shear modulus μ and a viscous element with viscosity η. Stress relaxation is governed by a single relaxation time, τ_M, defined as

$$\tau_M = \frac{\eta}{\mu}. \tag{10}$$

When fully relaxed, a Maxwell body has an effective shear strength of zero, as the elastic element no longer supports any stress. The standard linear solid considered here consists of a Kelvin element (elastic and viscous elements in parallel) in series with an elastic element. The Kelvin and individual elastic elements have shear moduli μ_k and μ_e, respectively, and the viscous element is again denoted by η. The characteristic times τ_K and τ_S are defined as

$$\tau_K = \frac{\eta}{\mu_k} \tag{11}$$

and

$$\tau_S = \frac{\eta}{(\mu_k + \mu_e)}. \tag{12}$$

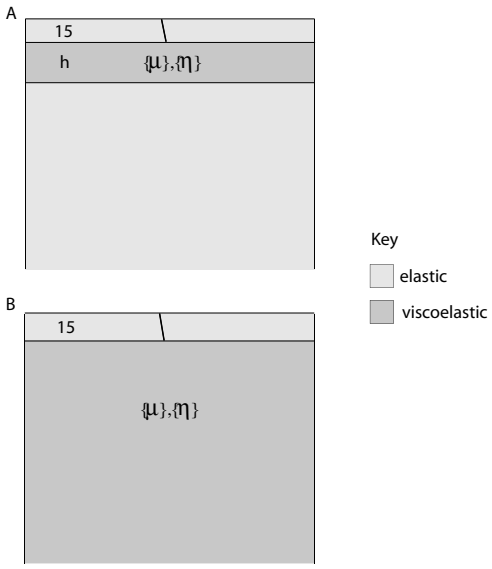

Rheology	Relaxation times	Long-term shear strength?
Maxwell 	$\frac{\eta}{\mu}$	NO
Standard Linear Solid 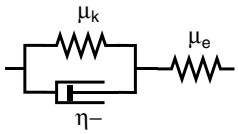	$\frac{\eta}{\mu_k}$ $\frac{\eta}{\mu_k + \mu_e}$	$\mu' = \frac{\mu_k \mu_e}{\mu_k + \mu_e}$

Figure 11. Top: Cross-sections of viscoelastic earth models used in the modelling. Model A: viscoelastic layer sandwiched between an elastic lid and an elastic half-space. The thickness (h) and material parameters ($\{\mu\},\{\eta\}$) of the layer are varied as explained in the text. Model B: elastic lid over viscoelastic half-space. The material parameters of the half-space are varied. In both models, the lid thickness is 15 km. Bottom: schematic illustration of simple mechanical analogues for Maxwell and standard linear solid rheologies.

A fully relaxed standard linear solid has non-zero effective shear modulus, μ':

$$\mu' = \frac{\mu_k \mu_e}{(\mu_k + \mu_e)}, \tag{13}$$

that is, the medium has long-term shear strength.

To investigate whether or not a simple viscoelastic layered model alone can explain the observed displacements, modelling was carried out using the Fortran codes V3FASAT (Fukahata & Matsu'ura 2006) and VISCO1D (Pollitz 1992). Preliminary modelling made use of V3FASAT, and the data-driven modelling described here uses VISCO1D. This code computes internal or surface displacements at user-specified times following the earthquake, for a user-specified earth model and set of fault parameters. The coseismic source parameters used were those obtained by Funning *et al.* (2006) from inversion of coseismic interferograms, assuming uniform slip on each of 11 segments (Table 3). The earth model consists of an elastic lid containing the fault rupture, and an underlying viscoelastic medium, whose rheological parameters are varied in each model run. The lid thickness is fixed at 15 km. This thickness is chosen because it is the depth above which most coseismic slip occurs (top panel of Fig. 17). It is well known that the crust beneath Tibet is 60–80 km thick. Zhu & Helmberger (1998) use broadband teleseismic body waves to estimate a crustal thickness of ∼70 km beneath the Kunlun mountains, and Braitenberg *et al.* (2002) estimate the same thickness in the Manyi area, from inversion of gravity data. The observed post-seismic displacements in the present study fall away to zero at a distance of about 70 km from the fault, that is, a distance less than the estimated thickness of the Tibetan crust in this region. The characteristics of the surface deformation field should, therefore, depend only on crustal rheology and be insensitive to the rheology of the upper mantle. Only the central, deforming portion of each time-series image was used (∼70 km either side of the fault), with down-sampling by a factor of ∼7 on a regular grid. The rms misfit between observations and model is calculated according to

$$\chi^2 = \frac{1}{n} \sum_{i=1}^{n} \left[(d_i - m_i)^2 \right], \tag{14}$$

where χ^2 is the misfit squared, n is the number of points on the ground, and d_i, m_i are the line-of-sight displacements for the i^{th} point on the ground for the data and model, respectively. For a range of viscosities between 10^{16} and 10^{21} Pa s, misfits are first computed at individual dates for each of the three tracks. At each time, cumulative line-of-sight displacements since the earthquake are considered. An overall misfit for each track is also computed, taking all dates collectively. We aim to determine whether or not either a Maxwell or standard linear solid rheology can explain the data over the entire observation period. For either model to be considered plausible, the best-fitting rheological parameters must be constant over time. For instance, if the Maxwell model is a plausible physical mechanism for the observed post-seismic motion, then the best-fitting viscosity for individual dates should be constant for the duration of the time-series.

5.2.2 Maxwell rheology

In modelling stress relaxation with a Maxwell rheology, the only parameter varied is the viscosity of the viscoelastic layer. The shear modulus is held constant at 5×10^{10} Pa. Two models are used, referred to as Models A and B (Fig. 11). In Model A, the lid overlies a viscoelastic layer, with an elastic half-space beneath. In Model B, the lid overlies a viscoelastic half-space. Model B is an end-member case of Model A, with an infinitely thick viscoelastic layer. In Model A, two different layer thicknesses are tried: a thin channel of 15 km and a thick channel of 50 km.

Curves of misfit as a function of viscosity are shown for Model B in Fig. 12. For both Models A and B, the viscosity preferred by the data increases by a factor of up to three over the observation period, depending on the track. The misfit curves are steeper at low viscosities, so there is a stronger lower bound to the apparent viscosity than upper bound. We assess whether the increase in apparent viscosity is significant by perturbing the time-series deformation with correlated noise (Parsons *et al.* 2005) and running the grid search 100 times. The time-series perturbation is carried out by first

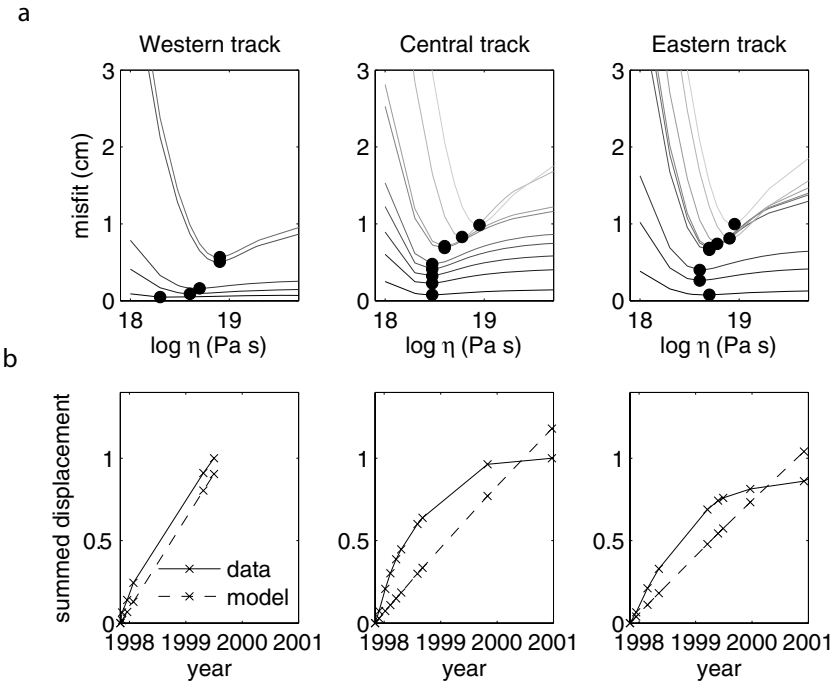

Figure 12. Results of Maxwell viscoelastic modelling. (a) Misfit as a function of viscosity for each of the three SAR tracks. Darker curves are dates early in the time-series and lighter curves are progressively later (see Table 2 for exact dates for each track). Dots mark the points of minimum misfit. The data require the viscosity to increase by a factor of three to four over the observation period. (b) Line-of-sight displacements summed over all pixels in each track. Solid lines show observed displacements and dashed lines show model displacements using the best fit viscosity for all time periods considered collectively. Both curves in each plot are normalized to the maximum observed displacement.

computing 1-D covariance functions for undeforming portions of each time-series image, in order to obtain quantitative approximations of realistic noise. These 1-D covariance functions are then used to create grids of correlated noise, which are added to the time-series images. Histograms of the best-fitting viscosity at different dates show that the increase in preferred viscosity is robust: the upper bound viscosity for the first date and the lower bound for the final date do not overlap. Histograms for Model B are shown in the left hand column of Fig. 14; those for Model A show a similar lack of overlap. This indicates that stress relaxation in a Maxwell medium beneath an elastic lid is not sufficient on its own to explain the time-series observations.

We now consider misfits computed for the entire time-series, that is, all dates are treated collectively rather than individually (Table 4). For each track, measured temporal decay curves are plotted against those predicted by the best-fitting overall model viscosity in Fig. 12(b). These curves are obtained by summing the absolute value of line-of-sight displacement over all points on the ground, and normalizing to the maximum observed value. Because the effective viscosity increases over the course of the time-series, using a single viscosity to generate the model decay curves results in a very poor fit to the data curves. Although the minimum misfit for Model A with a thin layer is only 5 mm less than that for Model A with a thick layer (Table 4), the vertical displacement fields predicted by the two models are very different and as a result the line-of-sight displacement fields differ significantly. A thin layer gives line-of-sight deformation lobes which thicken towards the east on both sides of the fault, whereas a thick layer gives a lobe which thickens to the east on the south side of the fault and to the west on the north side of the fault, as observed (Figs 5 and 7). We can, therefore, rule out a thin (15 km thick) viscoelastic layer. It is not possible, however, to distinguish between a 50 km-thick viscoelastic layer and a half-space. Surface deformation predicted by Maxwell viscoelastic half-space models is shown in Fig. 20 for two dates, along with the corresponding time-series images and the resulting residuals.

Table 4. Best-fitting viscosities and misfits computed over all dates collectively, for the Maxwell Models A and B.

Model	Viscosity (Pa s)	Misfit (cm)
A (thin layer)	5×10^{18}	0.65
A (thick layer)	7×10^{18}	0.60
B	7×10^{18}	0.58

5.2.3 Standard linear solid rheology

For the standard linear solid case, the parameters varied are the viscosity, η, and the shear modulus of the Kelvin elastic element, μ_k (see Fig. 11). The value of the shear modulus of the other elastic element, μ_e, is held constant at 5×10^{10} Pa. In this section, only a half-space beneath an elastic lid is considered. Again, misfits are computed for individual dates. The value of μ_k which gives the lowest misfits is 2.4×10^{10} Pa; the misfit–viscosity curves for this value of μ_k are shown in Fig. 13. The overall best-fitting viscosity is 4×10^{18} Pa s, and, in contrast to the results of the Maxwell modelling, here the data only require a slight increase in viscosity over the observation period. The histogram series in the right hand column of Fig. 14 shows a less decisive increase in viscosity towards the end of the time-series, relative to the Maxwell equivalent. The temporal decay curves predicted by the best-fitting overall viscosity for each track agree very well with the time-series curves, departing slightly in the final year. These results imply that a standard linear solid

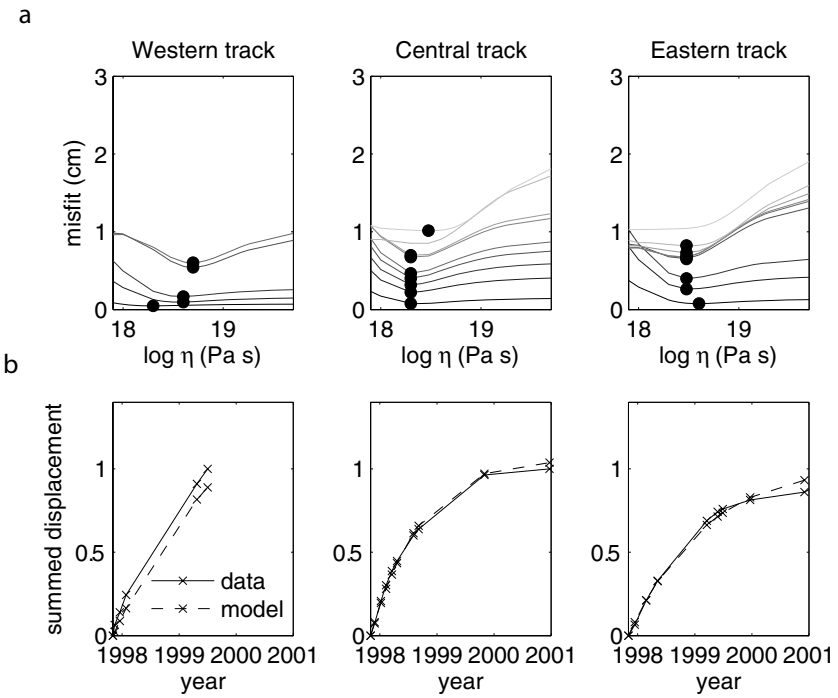

Figure 13. Results of standard linear solid viscoelastic modelling. Curves as for Fig. 12.

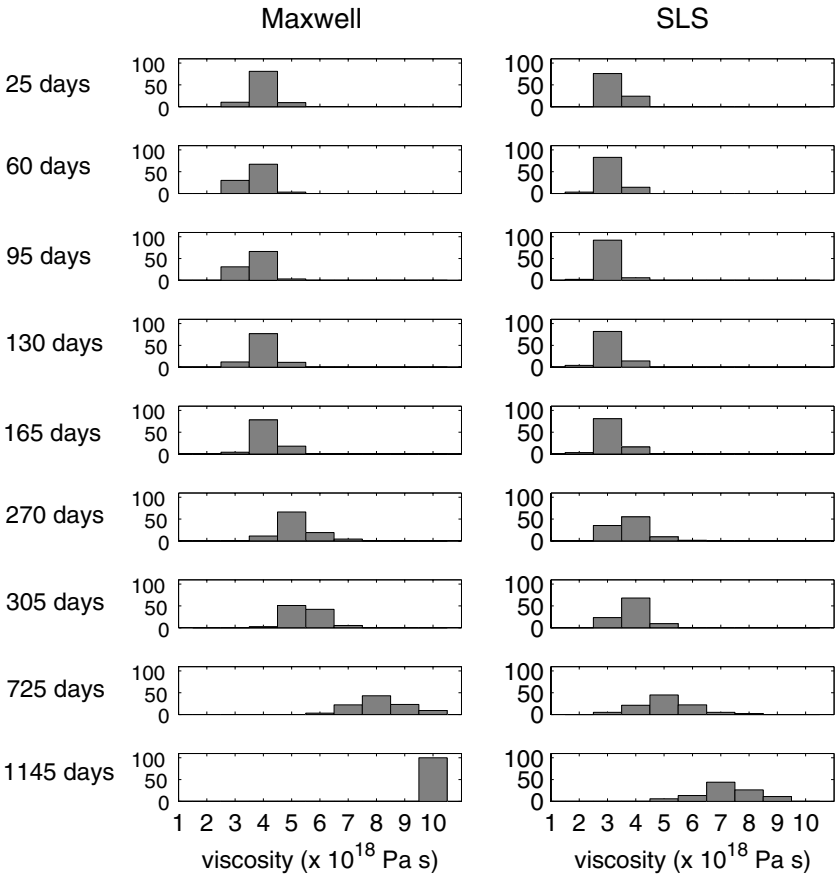

Figure 14. Histograms of best-fitting viscosity for different dates, for the central track. Maxwell results for Model B are in left hand column and standard linear solid (SLS) results are in right hand column. The histograms were constructed by perturbing the time-series deformation with realistic noise and finding the best-fit viscosity using the viscoelastic model outputs 100 times, as described in the text. The lack of overlap between the range of viscosities for first and last dates shows that the preferred increase in apparent viscosity with time is a robust conclusion.

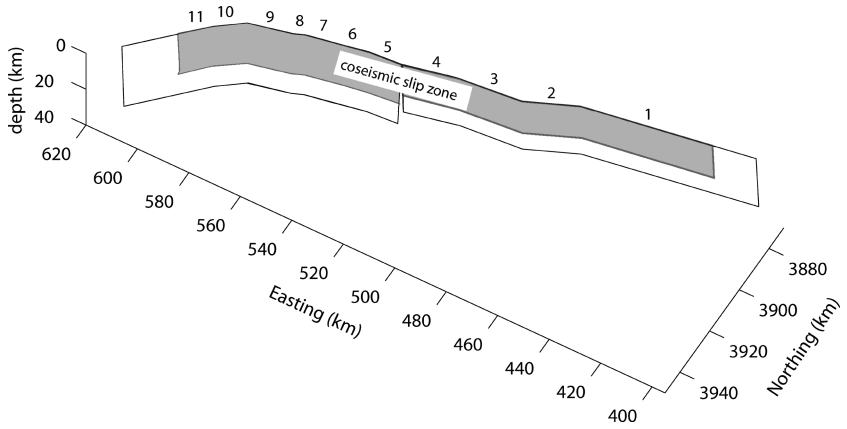

Figure 15. Geometry and orientation of slip zone used in inversions. Coseismic fault parameters and segment numbers are taken from Funning *et al.* (2006). The extensions at depth and at the ends of the fault extrapolate the coseismic dip and strike.

is superior to a Maxwell solid in approximating the lower crustal rheology in this part of Tibet. Surface deformation predicted by the best-fitting standard linear solid rheology is shown in Fig. 20 for two dates, along with the corresponding time-series images and the resulting residuals. The modelled line-of-sight displacements have an asymmetrical pattern across the fault similar to that observed (see Section 4). The fit between observed and modelled displacements is particularly good on the northern side of the fault.

5.3 Afterslip modelling

5.3.1 Method

For this part of the modelling we assume that afterslip on the fault and its extension at depth is responsible for post-seismic motion. Any stress increases on or at the margins of a fault plane can potentially be relieved by slip across a surface or thin shear zone. To investigate the development of the slip distribution that would give rise to the observed surface deformation field, we invert the time-series at successive dates. It is preferable to use all three tracks of data in the inversion, rather than inverting one at a time. In order to do this, the western and eastern time-series are interpolated temporally, using cubic splines, so that their dates match those of the central time-series. As for the viscoelastic modelling, the time-series images are down-sampled by a factor of $\sim$7 on a regular grid. Gradient-based resampling (e.g. Jonsson *et al.* 2002) is not deemed necessary: profiles across the deforming region reveal fairly low gradients of deformation—the highest gradient in the profile in Fig. 5 is 94 mm km^{-1}, about 25 times lower than coseismic gradients near the surface break discontinuity. The earth is assumed to be an elastic half-space with no rheological layering. The fault geometry used is that obtained by Funning *et al.* (2006) from inversion of coseismic interferograms. Slip is allowed to occur on the coseismic fault plane and an extension of it at each end by 20 km and at depth (Fig. 15). A Green's function approach is used, where first the displacement due to one metre of slip on each fault patch is computed to give matrix **G**. The basic linear matrix equation to be solved is

$$\mathbf{Gm} = \mathbf{d}, \tag{15}$$

where **d** is the data, that is, line-of-sight displacement, and **m** is the model solution, that is, slip. Laplacian smoothing is applied between adjacent fault patches, so as to avoid unphysically large variations in the slip distribution:

$$\nabla^2 m = \mathbf{0}. \tag{16}$$

The finite difference approximation of the Laplacian, ∇^2, is weighted by the smoothing factor α^2, such that we now have

$$\left[\mathbf{F}\right]\left[\mathbf{m}\right] = \begin{bmatrix} \mathbf{G} \\ \alpha^2\nabla^2 \end{bmatrix}\left[\mathbf{m}\right] = \begin{bmatrix} \mathbf{d} \\ \mathbf{0} \end{bmatrix}. \tag{17}$$

The kernel **F** is weighted by the inverse of the data covariance matrix Σ_{d}, computed separately for each date in the time-series from the undeforming parts of the images. This approach takes into account the correlated nature of noise in the interferograms, and hence in the time-series, so as to give realistic error estimates in the slip distribution. It also prevents biasing of the model from correlated data points in the far-field. Additional terms to account for linear ramp and constant offset are also included (not shown). This is to minimize the effect on the solution of any residual long-wavelength orbital signal that was not removed by the corrections described in Section 3 above. The model solution, **m**, is obtained by a non-negative least-squares algorithm, with the optimal value of α being determined by the point of maximum curvature of a roughness versus misfit plot. The rake, ϕ, for each patch is allowed to vary between 45° either side of pure left lateral. For each slip patch, the solution yields one slip vector magnitude for rake $-45°$ and one for rake 45°. Since the solution is non-negative, this gives an overall rake of $|\phi| < 45°$. Model errors are estimated by adding spatially correlated noise to the time-series, as described in Section 5.2.2, and running the inversion 100 times. For any given patch, this yields two distributions of slip values, one for each rake component. The overall error is the norm of the standard deviation of these distributions.

Afterslip is allowed to occur on an extension of the coseismic rupture surface at depth. The depth to which slip should be allowed to occur is not immediately obvious from physical reasoning. Other studies of post-seismic afterslip have simply imposed an arbitrary maximum depth. We address the question of to what depth slip should be allowed to occur by running the inversion for a range of different depths, between 10 and 80 km. Tests with synthetic data show that it is possible to estimate the appropriate inversion depth from consideration of rms misfit. Known slip distributions on surfaces down to different depths are used to generate synthetic interferograms, with an approximately elliptical slip distribution in the lower half of any given surface. Noise is then added to the synthetic interferograms. The spatial correlation of the synthetic

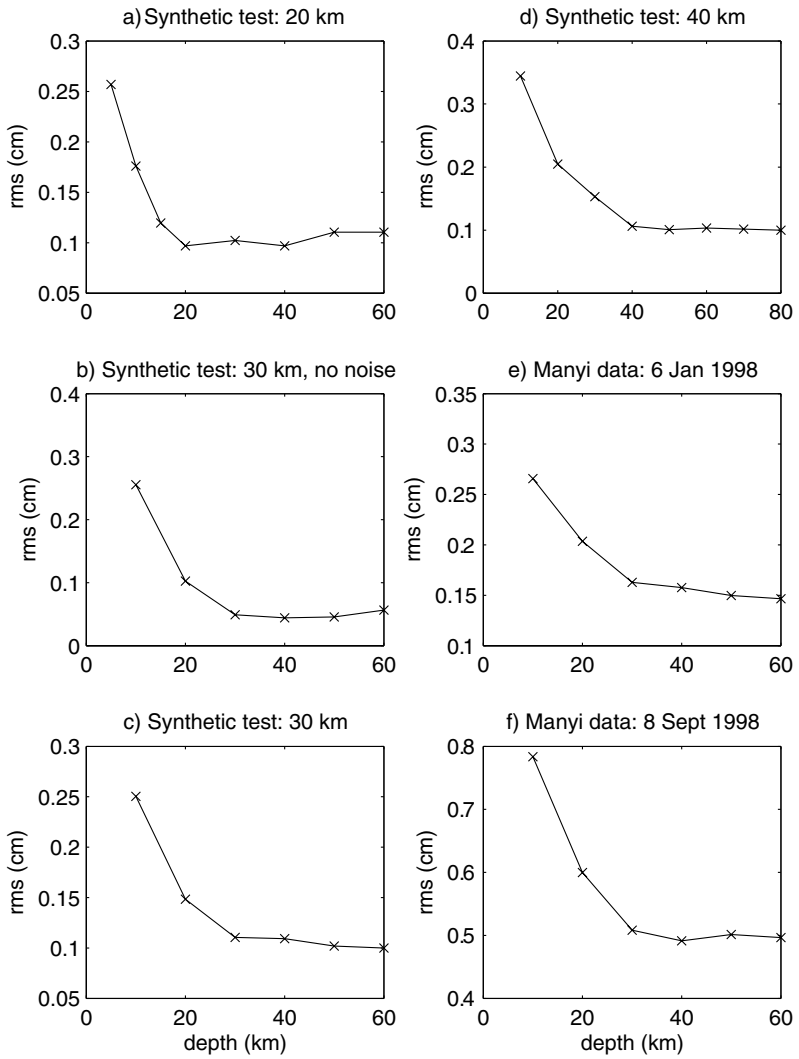

Figure 16. Plots of rms misfit against inversion depth. (a) Synthetic slip distribution down to 20 km. (b) Synthetic slip distribution down to 30 km, with no noise added. (c) Synthetic slip distribution down to 30 km, with noise added. (d) Synthetic slip distribution down to 40 km. (e) Second date of Manyi time-series (6 January 1998). (f) Seventh date of Manyi time-series (1998 September 8).

noise is as calculated for the Manyi area in Section 5.2.2, and the maximum amplitude of the noise is set to be about one tenth of the maximum signal size. When the allowed depth is shallower than the imposed slip, the inversion does a poor job of matching the synthetic data, so the rms misfit is large. As the inversion depth increases, the fit improves, up to the point of the actual maximum slip depth, when the misfit levels off. Fig. 16 shows inversion depth-misfit plots for three different synthetic experiments with known slip distributions. The 30 km case is run both with and without noise. In each case the correct depth is picked out by the point at which the plot levels off. Plots for the Manyi data are also shown, for two dates in the time-series, one early and one later. The appropriate inversion depth indicated by the plots is 30 km. It is assumed that slip does not get deeper or shallower with time, so slip is allowed down to 30 km for the whole time-series.

5.3.2 Results

The post-seismic afterslip distribution time-series is shown in Fig. 17, along with the coseismic slip distribution, as obtained by Funning *et al.* (2006). In general, slip increases with time, at a decreasing rate, but the slip pattern is spatially fairly stable over time. After 3 yr, the maximum slip magnitude is 0.72 m, and the moment release is 6.4×10^{19} N m, approximately 20 per cent of the coseismic moment. The rms misfit averaged over all dates is 0.37 cm. The position of the post-seismic slip maximum corresponds to that of the coseismic maximum lengthwise along the slip zone. Depthwise, afterslip occurs mainly beneath the zone of coseismic slip. Bearing in mind that, apart from the fault geometry, the post-seismic inversions were carried out without reference to the coseismic source model, these spatial relationships seem to support the possibility of afterslip being a plausible mechanism. Fig. 18 illustrates how slip changes as a function of time, for all patches collectively (top panel) and for individual patches (middle panel). The decay time found by summing the absolute range change over all pixels and fitting an exponential curve of the form $B(1 - e^{-t/T})$, where B and T are constants and t is time, is 1.6 yr. This is more than twice the decay time computed for summed surface deformation (Section 4). As with the decay of surface displacements, no physical significance is attached to the exponential functionality. The exponential decay time

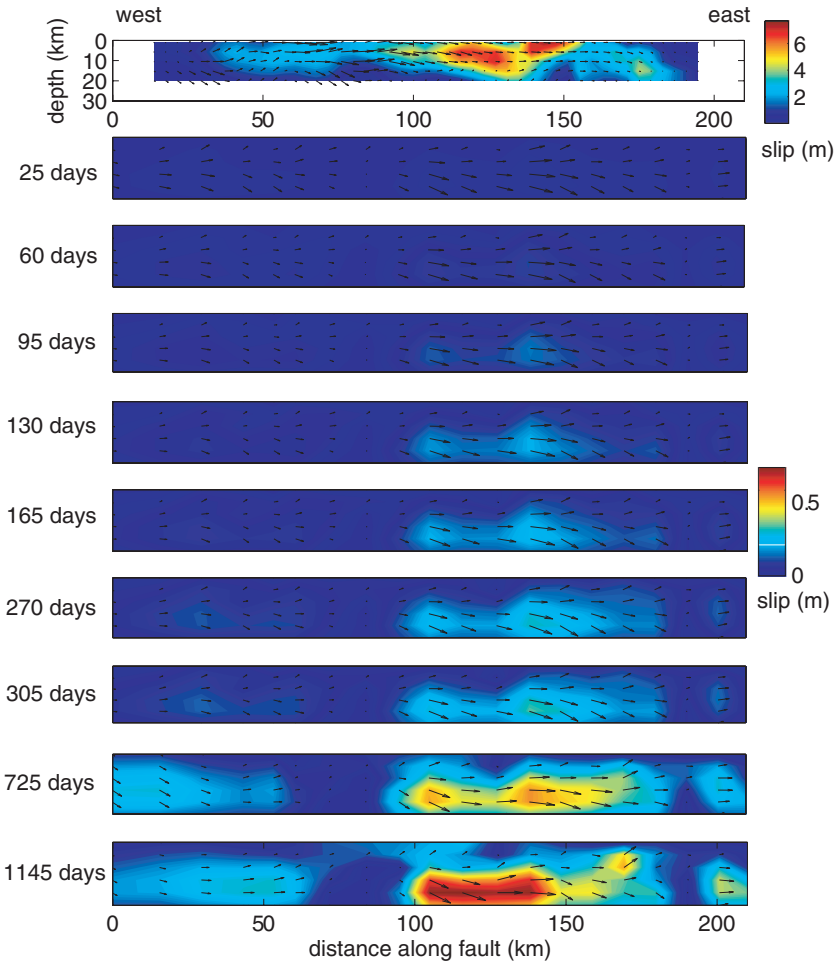

Figure 17. Coseismic and post-seismic slip distributions. View is from the south. For clarity, fault segments are shown as a single plane, rather than in the actual fault geometry shown in Fig. 15. The coseismic slip distribution, as obtained by Funning *et al.* (2006), is shown at the top and the time-series of post-seismic slip distributions is shown beneath. Note the different colour scales for the coseismic and post-seismic slip distributions. All three tracks are used in the inversion, except for the final two dates, when only the central and eastern tracks are used: the dates of the western track are all pre-2000 (see Fig. 3).

calculated for individual slip patches ranges fairly evenly from 0 to 10 yr, with no modal value. The surface line-of-sight displacement field predicted by afterslip forward models is shown in Fig. 20 for two dates, along with the corresponding time-series images and the associated residuals. The highest residuals occur at the eastern end of the fault, both for the afterslip and viscoelastic models, and afterslip model errors are also highest at this end. Funning *et al.* (2006) likewise find that the highest residuals for their coseismic inversions occur at the eastern end. Despite very detailed mapping of the fault trace from satellite images by Funning *et al.* (2006), these authors point out that locating a definitive fault trace at the eastern end is problematic, due to a lack of convincing geomorphological or offset features. It may be that modifying the position and orientation of the easternmost segments of Table 3 and Fig. 15 would reduce the residuals, but we do not attempt to do so here. The observed asymmetry in the line-of-sight displacements across the fault are not particularly well reproduced by the afterslip model. The displacement pattern south of the fault is matched better by afterslip than by viscoelastic relaxation. North of the fault, neither model provides a strong match through 1998, but from 1999 onwards the observations are better matched by viscoelastic relaxation than by afterslip.

Fig. 19 shows 1σ errors in the slip distribution, calculated as described in Section 5.3.1, for September 8 1998 (305 d after the earthquake). In general, errors are smaller for the shallow patches and larger deeper down. For this date the maximum error is 12 cm. The errors for the western part of the slip zone are large for the last two dates in the time-series (not shown), because for these dates, only the central and eastern tracks provide data this late after the earthquake.

To investigate whether post-seismic slip regions correspond to zones of earthquake-induced shear stress increase, we compute horizontal shear stress changes caused by the coseismic rupture on the afterslip surface (Fig. 21a). In general, there is a shear stress decrease in areas of coseismic slip and a shear stress increase in adjacent areas. Fig. 21(b) is a reproduction of the first plot in the post-seismic slip time-series of Fig. 17, with a different colour scale. Comparison of Figs 21(a) and (b) reveals a first order along-strike correlation between areas of high shear stress change and afterslip. However, the correlation between coseismic and post-seismic slip mentioned above is more convincing. The background tectonic stress is unknown, but is almost certainly spatially variable. Aseismic slip likely occurs in zones of high absolute stress rather than in zones of coseismic stress increase (Fialko 2004b).

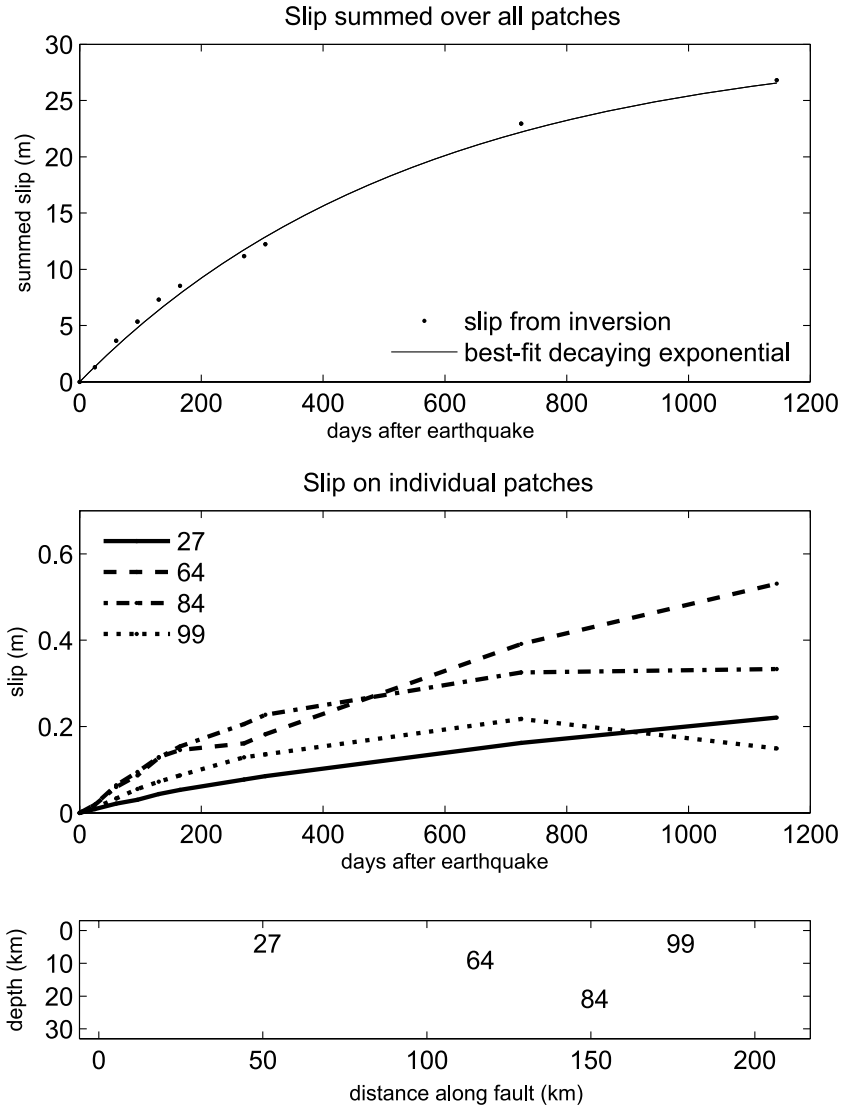

Figure 18. Slip as a function of time. Top panel: slip summed over all fault patches. The dots show the slip obtained from the inversions, and the curve is the best-fitting decaying exponential, with a decay time of 1.6 yr. Middle panel: slip for four individual fault patches, numbered and marked in the lower panel.

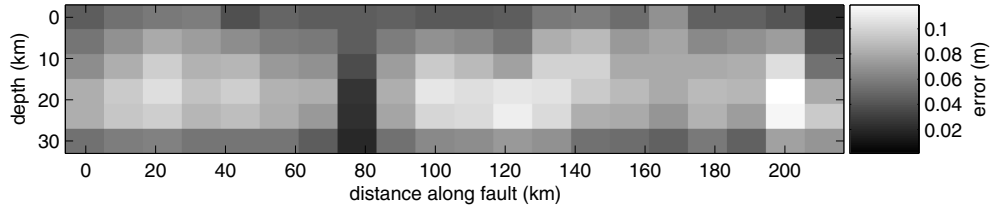

Figure 19. Estimated errors in the slip values for the 305 day inversion solution.

6 DISCUSSION

The observed and modelled line-of-sight displacement fields shown in Fig. 20 highlight the fact that different mechanisms acting at depth can give rise to very similar displacement fields at the surface (e.g. Savage 1990; Hearn 2003). Here we discuss the plausibility of different mechanisms. Crustal and upper mantle rheological properties in this part of Tibet are not well-known, since most regional lithospheric studies concentrate on the Kunlun Fault to the east, the Karakorum Fault to the west, or do not extend far enough north. However, the plateau-scale mid to lower crustal and upper mantle partial melt zone identified by International Deep Profiling of Tibet and the Himalaya (INDEPTH) transects (Wei *et al.* 2001) may well apply to the Manyi area. Such a zone of partial melt is supported by the presence of Plio-Pleistocene potassic volcanism north of the Manyi fault and 4 Ma rhyolites at Ulugh Muztagh (Fig. 1) (Ding *et al.* 2003). It is not possible to directly relate conductivity values to viscosities, but zones of higher conductivity likely correlate to first order with zones of lower viscosity (A. Jones, personal communication, 2005). As the conductance of the mid to lower

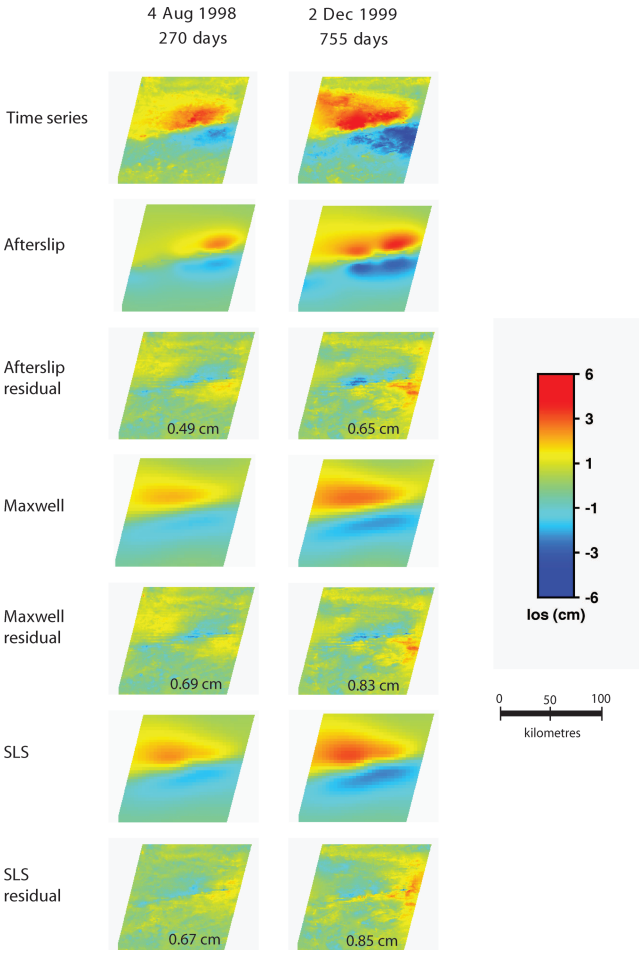

Figure 20. Observations compared with viscoelastic and afterslip model outputs for the central track (track 305), for two of the dates in the time-series. Residuals are also shown. Values given in the residual images are rms misfits. The viscoelastic synthetics are computed using the best-fitting viscosity appropriate to each individual date, rather than the overall best-fitting viscosity.

Tibetan crust is one to two orders of magnitude greater than that of typical continental regions (Wei *et al.* 2001), it is plausible that mid to lower crustal viscosity is significantly lower.

The Manyi post-seismic deformation can be matched fairly well by a model consisting of a standard linear solid half-space (mid to lower crust) beneath an elastic lid (upper crust). The viscoelastic half space is characterized by three material constants: the shear modulus of the purely elastic component, which gives rise to an instantaneous response, and the shear modulus and viscosity of the Kelvin component, which has a delayed response. In this particular case, the relaxed shear modulus (see eq. 13) is 32 per cent of the purely elastic value; in other words, the mid to lower crust has, according to this model, significant long-term strength. A handful of other studies have considered a standard linear solid rheology (e.g. Nur & Mavko 1974; Cohen 1982; Pollitz & Sacks 1996; Pollitz *et al.* 2000). In a modelling study of time-dependent deformation following strike-slip earthquakes, Cohen (1982) has a standard linear solid layer sandwiched between an elastic lid and a Maxwell layer. He justifies the choice of standard linear solid by categorizing it as transitional between the elastic lid, which can support long-term stresses, and the underlying Maxwell layer, which cannot. Both Pollitz & Sacks (1996) and Pollitz *et al.* (2000) require non-zero values of relaxed shear modulus for the lower crust, in studies of post-rifting deformation in Iceland and post-seismic deformation after the Landers earthquake, respectively.

The best Maxwell models described in Section 5.2.2 do not give a satisfactory fit to observed displacements following the Manyi earthquake. The results imply that effective viscosity increases with time. How is this consistent with the standard linear solid model, where the viscosity is more or less constant over time? If we consider the relaxation time,

$$\tau = \frac{\eta}{\mu}, \tag{18}$$

rather than the viscosity itself, then we can see that in the Maxwell case, in order to fit the Manyi post-seismic data, τ increases with time by a factor of about three. In the standard linear solid case, the shear modulus governing the system is initially μ_e, and it falls to μ' as stresses relax: at the start and end of relaxation, there is a single governing shear modulus, so in each case we can apply the simple formulation of eq. (18). Thus, τ increases with time, again by a factor of about three; in this case the increase is a result of μ falling rather than η rising. This simple analysis shows that the results of the two rheological models are consistent. The key point of the viscoelastic modelling results is that the observed transient signal demands two relaxation times. Rather than concluding that the lower crust behaves exactly like a standard linear solid, we prefer simply to emphasize the rapid initial response followed by the slower response later on. If the lower crust does in fact behave like a standard linear solid, then lower crustal stresses should increase after the transient phase of each earthquake. This suggests that, on a longer timescale than that of the observations presented here, some relaxation process acts to decrease the long-term shear modulus.

The increase in effective viscosity suggested by the time-series could arise from a non-linear viscoelastic system. Non-linear modelling is beyond the scope of this paper, though the results of the afterslip modelling are not altogether incompatible with a non-linear rheology, as explained below. Another possibility is a Burgers rheology, as proposed by Pollitz (2005) for the upper mantle to explain transient ground motion following the 2002 Denali earthquake, Alaska. A Burgers body consists of a Maxwell element in series with a Kelvin element, each element having its own associated relaxation time: the Kelvin part is responsible for the rapid initial motion and the Maxwell part for the subsequent slower motion. The simple analysis carried out here, using the two viscoelastic models with the fewest parameters, could be extended to test the biviscous Burgers rheology.

The results of the afterslip inversions suggest that aseismic slip is a reasonable mechanism for explaining the observed surface motion. Although the inversions are purely kinematic, zones of high coseismic slip correlate along strike with zones of high afterslip, and the afterslip in general occurs beneath the depth of coseismic rupture. Dynamic modelling of afterslip, taking rate and state friction laws into consideration (Johnson *et al.* 2006), may shed further light on this issue. Our simple model does not attempt to distinguish between slip on a discrete surface and motion across a narrow ductile shear zone; overlying elastic material would filter out any differences in short wavelength signal between the two models, rendering them indistinguishable at the surface. With power-law behaviour, viscosity decreases most where stresses increase most, and as these stresses are relaxed, viscosity increases. For the early stages of relaxation, non-linear viscoelasticity can be regarded as an approximation to afterslip (Fialko 2004a), since the stress dependence of viscosity has the effect of localizing deformation into the narrow zone beneath

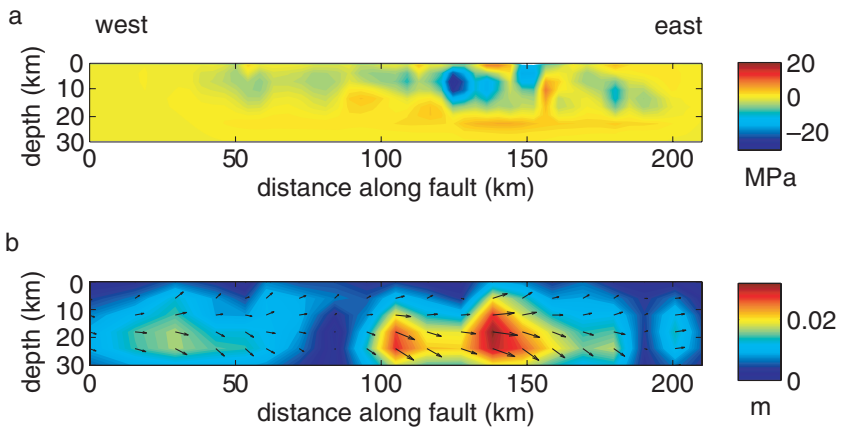

Figure 21. (a) Horizontal shear stress changes induced by the earthquake rupture. Source model is taken from Funning *et al.* (2006). (b) Post-seismic slip distribution for first date in time-series (25 days after the earthquake).

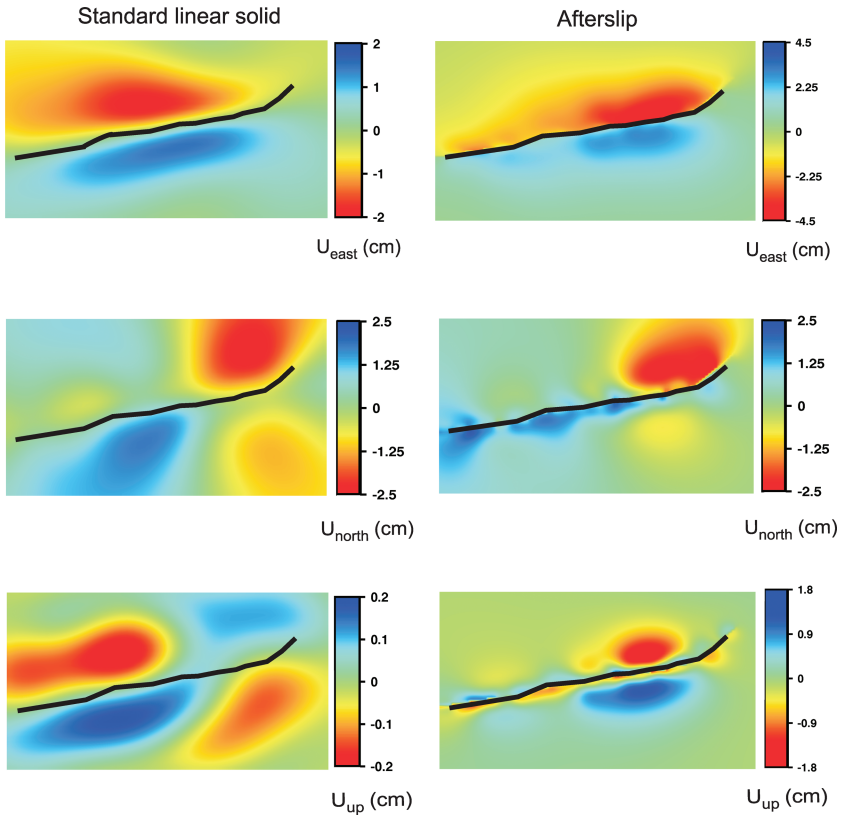

Figure 22. Displacement components (U) predicted by the standard linear solid viscoelastic relaxation model (left) and the afterslip model (right). Displacements are computed at 270 days after the earthquake. Black line marks fault.

the coseismic rupture, where stress increases are highest. Power-law flow was proposed by Freed & Bürgmann (2004) as a viable mechanism to explain post-seismic transients following the Hector Mine and Landers earthquakes in California. Newtonian modelling (where the power-law exponent is set to 1, so that effective viscosity is stress- and time-independent) made it impossible to match both the rapidly decaying early signal and the more slowly decaying late signal with a single viscosity. Power-law flow is also found to provide a good fit to post-Denali earthquake GPS displacements by Freed *et al.* (2006).

The task of distinguishing afterslip and viscoelastic relaxation is made easier by the availability of separate horizontal and vertical displacement components. For strike-slip faults, horizontal displacements caused by the two mechanisms tend to have a similar spatial pattern, while the vertical components have opposite sign. For certain fault and satellite geometries, this means that line-of-sight displacements predicted by afterslip and viscoelastic relaxation are also anti-correlated. This was the case for the 1999 Hector Mine earthquake Pollitz *et al.* (2001), and as a result viscoelastic relaxation could be identified as the dominant mechanism. For the Manyi

case, there are no GPS data available in this part of Tibet, and there are no ascending SAR scenes, so it is not possible to resolve horizontal and vertical motions. Furthermore, the relative orientation of the Manyi fault and the ERS-2 look direction means that the observed line-of-sight displacement field does not have a clear-cut quadrant pattern. Although we cannot distinguish between horizontal and vertical components in the time-series, the behaviour of the different components of motion is nonetheless of interest. Horizontal and vertical displacement components predicted by the afterslip and standard linear solid models are shown in Fig. 22 for day 270. The easterly components for the two models show a similar left-lateral pattern. The northerly components are similar at the eastern end and dissimilar at the western end, with more short-wavelength features near the fault in the afterslip case. The vertical components are markedly different everywhere. The varying strike of the fault and the varying dip along strike mean that there is not a straightforward quadrant pattern to the vertical displacements. To first order, the afterslip displacements are an order of magnitude larger than the viscoelastic relaxation displacements, and the two displacement fields are anticorrelated towards the eastern end of the study area. Although line-of-sight displacements are most sensitive to vertical motions, it should be noted that viscoelastic models predict vertical displacement components which are much smaller than the horizontal components. Again, there is more near-fault detail in the afterslip case.

Where do aftershocks fit into this picture? As mentioned in Section 2, the Manyi aftershocks are very small in magnitude, which suggests that strain was released efficiently by the main shock (Velasco *et al.* 2000). This is not at odds with the significant post-seismic (non-aftershock) signature. Physically, it is possible to have strain released efficiently in the upper, elastic portion of the crust, with the bottom portion then adjusting in response to local stress changes. According to the brittle creep mechanism modelled by Perfettini & Avouac (2004), aftershocks and deep afterslip follow the same temporal evolution. These authors confirm this correlation for the 1999 Chi-Chi earthquake. For the Manyi earthquake, the correlation does not apply: the rate of aftershocks decays more rapidly than the afterslip. If afterslip occurs for a short while at the beginning of the post-seismic period, superimposed on viscoelastic relaxation, the relationship could still hold; it is simply masked in this case by the longer timescale viscous adjustment occurring as well.

7 CONCLUSIONS

This study has shown that significant post-seismic motion occurred in the 4 yr following the Manyi earthquake in 1997. InSAR observation has revealed up to ± 5 cm of deformation, extending to distances of about 70 km from the fault, with peak deformation occurring at 10–20 km from the fault. We have investigated the spatial and temporal characteristics of four possible causal mechanisms: poroelastic rebound, Maxwell and standard linear solid viscoelastic relaxation, and afterslip. We conclude that two of these mechanisms can explain the observed time-series, even if the physical rationale behind them is not fully understood. Stress relaxation in a standard linear solid rheology models the data satisfactorily, with a best-fitting viscosity of 4×10^{18} Pa s and a fully relaxed shear modulus which is 32 per cent of the purely elastic value. The rapid initial response and the slower response after the first year can be characterized by the two relaxation times. Time-series inversions for afterslip on an extension of the fault plane at depth give slip distributions which correlate along strike with coseismic slip, suggesting that this is a feasible process. Afterslip modelling gives a maximum slip of 0.72 m after 3 yr, and the equivalent moment release is approximately 20 per cent of the coseismic moment. The poroelastic rebound model produces a spatial deformation pattern unlike that observed, while a Maxwell viscoelastic half-space (or thick layer) provides a reasonable spatial fit to the data, but cannot match the temporal behaviour of the surface deformation. The thick Tibetan crust and the presence of recent volcanism in the Manyi region is consistent with a viscoelastic rheology. A more extended period of post-seismic observation, along with data from ascending SAR tracks, might enable proposed mechanisms to be distinguished.

ACKNOWLEDGMENTS

This work was supported by the Natural Environment Research Council (NERC) through the Centre for the Observation and Modelling of Earthquakes and Tectonics (COMET) and a tied studentship to IR. The ERS SAR data are copyrighted by the European Space Agency and were provided under project AOE-621. We would like to thank Fred Pollitz for making his code VISCO1D freely available; Philip England, Roland Bürgmann, Yukitoshi Fukahata and Sigurjón Jónsson for useful discussions; Juliet Biggs for suggesting early improvements to the manuscript; and Wayne Thatcher and Yuri Fialko for providing useful reviews.

REFERENCES

Berardino, P., Fornaro, G., Lanari, R. & Sansosti, E., 2002. A New Algorithm for Surface Deformation Monitoring Based on Small Baseline Differential SAR Interferograms, *IEEE Trans. Geosci. Remote Sens.,* **40, 11,** 2375–2383.

Braitenberg, C., Wang, Y., Fang, J. & Hsu, H.T., 2002. Spatial variations of flexure parameters over the Tibet-Quinghai plateau, *Earth planet. Sci. Lett.,* **6464,** 1–14.

Bürgmann, R., Ergintav, S., Segall, P., Hearn, E., McClusky, S., Reilinger, R.E., Woith, H. & Zschau, J. 2002. Time-Space Variable Afterslip on and Deep Below the Izmit Earthquake Rupture, *Bull. seism. Soc. Am.,* **92,** 126–137.

Cohen, S.C., 1982. A multilayer model of time dependent deformation following an earthquake on a strike slip fault. *J. geophys. Res.,* **87,** 5409–5421.

Deng, J., Gurnis, M., Kanamori, H. & Hauksson, E., 1998. Viscoelastic flow in the lower crust after the 1992 Landers, California, earthquake, *Science,* **282,** 1689–1692.

Ding, L., Kapp, P., Zhong, D. & Deng W., 2003. Cenozoic Volcanism in Tibet: Evidence for a Transition from Oceanic to Continental Subduction, *J. Petrology,* **44, 10,** 1833–1865.

Ergintav, S. *et al.*, 2002. Postseismic deformation near the Izmit earthquake (17 August 1999, M 7.5) rupture zone, *Bull. seism. Soc. Am.,* **92,** 194–207.

Farr, T.G. & Kobrick, M., 2000. Shuttle Radar Topography Mission produces a wealth of data, *EOS, Trans. Am. geophys. Un.,* **81,** 583–585.

Fialko, Y., 2004a. Spatio-temporal signatures of post-seismic relaxation due to the Mojave desert (S. California) earthquakes from InSAR and GPS data, with implications for the driving mechanisms, *EOS, Trans. Am. geophys. Un.,* **Suppl. abst.**, G12A-04.

Fialko, Y., 2004b. Evidence of fluid-filled upper crust from observations of postseismic deformation due to the 1992 M(w)7.3 Landers earthquake, *J. geophys. Res.,* **109,** B08401.

Freed, A.M. & Bürgmann, R., 2004. Evidence of power-law flow in the Mojave desert mantle, *Nature,* **430,** 548–551.

Freed, A.M., Bürgmann, R., Calais, E. & Freymueller, J., 2006. Stress-dependent power-law flow in the upper mantle following the 2002 Denali, Alaska, earthquake, *Earth Planet. Sci. Lett.,* **252,** 481–489.

Fukahata, Y. & Matsu'ura, M., 2006. Quasi-static internal deformation due to a dislocation source in a multilayered elastic/viscoelastic half-space and an equivalence theorem, **166,** 418–434.

Fukahata, Y., Nishitani, A. & Matsu'ura, M., 2004. Geodetic data inversion using ABIC to estimate slip history during one earthquake cycle with viscoelastic slip-response functions, *Geophys. J. Int.,* **156,** 140–153.

Funning, G.J., Parsons, B. & Wright, T.J., 2006. The 1997 Manyi, Tibet earthquake: linear elastic modelling of InSAR data, *Geophys. J. Int.,* accepted.

Gavrilenko, P., 2005. Hydromechanical coupling in response to earthquakes: on the possible consequences for aftershocks. *Geophys. J. Int.,* **161, 1,** 113–129.

Hearn, E.H., 2003. What can GPS data tell us about the dynamics of post-seismic deformation? *Geophys. J. Int.,* **155,** 753–777.

Hearn, E.H., Bürgmann, R. & Reilinger, R.E., 2002. Dynamics of Izmit Earthquake Postseismic Deformation and Loading of the Düzce Earthquake Hypocenter. *Bull. seism. Soc. Am.,* **92,** 172–193.

Jacobs, A., Sandwell, D., Fialko, Y. & Sichoix, L., 2002. The 1999 Mw 7.1 Hector Mine, California, Earthquake: Near-Field Postseismic Deformation from ERS Interferometry, *Bull. seism. Soc. Am.,* **92, 4,** 1433–1442.

Johnson, K.M., Bürgmann, R. & Larson, K., 2006. Properties on the San Andreas Fault Near Parkfield, California Inferred from Models of Afterslip Following the 2004 Earthquake, *Bull. seism. Soc. Am.,* **96,** 321–338.

Jonsson, S., Zebker, H.A., Segall, P. & Amelung, F., 2002. Slip distribution ofthe 1999 M7.1 Hector Mine earthquake determined from geodetic data, *Bull. seism. Soc. Am.,* **92,** 1377–1389.

Jónsson, S., Segall, P., Pederson, R. & Bjornsson, G., 2003. Post-earthquake ground movements correlated to pore-pressure transients, *Nature,* **424,** 179–183.

Kisslinger, C. & Jones, L.M., 1991. Properties of aftershocks in southern California. *J. geophys. Res.,* **96,** 11 947–11 958.

Masterlark, T. & Wang, H., 2000. Poroelastic Coupling Between the 1992 Landers and Big Bear Earthquakes, *Geophys. Res. Lett.,* **27, 22,** 3647–3650.

Massonnet, D., Feigl, K., Rossi, M. & Adragna, F., 1994. Radar interferometric mapping of deformation in the year after the Landers earthquake. *Nature,* **369,** 227–230.

Massonet, D., Thatcher, W. & Vadone, H., 1996. Detection of postseismic fault-zone collapse following the Landers earthquake, *Nature,* **382,** 612–615.

Nur, A. & Mavko, G., 1974. Postseismic viscoelastic rebound. *Science,* **183,** 204–206.

Parsons, B, *et al.,* 2005. The 1994 Sefidabeh (eastern Iran) earthquakes revisited: new evidence from satellite radar interferometry and carbonate dating about the growth of an active fold above a blind thrust fault, *Geophys. J. Int.,* **164,** 202–217.

Peltzer, G., Rosen, P., Rogez, F. & Hudnut, K., 1996. Postseismic Rebound in Fault Step-Overs Caused by Pore Fluid Flow. *Science,* **273, 5279,** 1202–1204.

Peltzer, G., Crampé, F. & King, G., 1999. Evidence of Nonlinear Elasticity of the Crust from the Mw 7.6 Manyi (Tibet) Earthquake, *Science,* **286,** 272–275.

Perfettini, H. & Avouac, J.P., 2004. Postseismic relaxation driven by brittle creep: A possible mechanism to reconcile geodetic measurements and the decay rate of aftershocks, application to the Chi-Chi earthquake, Taiwan. *J. geophys. Res.,* **109, B2,** B02304.

Pollitz, F. 1992. Postseismic relaxation theory on a spherical earth. *Bull. seism. Soc. Am.,* **82, 1,** 422–453.

Pollitz, F., 2005. Transient rheology of the upper mantle beneath central Alaska inferred from the crustal velocity field following the 2002 Denali earthquake, *J. geophys. Res.,* **110,** B08407.

Pollitz, F.F. & Sacks, I.S., 1996. Viscosity structure beneath northeast Iceland, *J. geophys. Res.,* **101,** 17 771–17 793.

Pollitz, F., Peltzer, G. & Bürgmann, R., 2000. Mobility of continental mantle: evidence from postseismic geodetic observations following the 1992 Landers earthquake. *J. geophys. Res.,* **105,** 8035–8054.

Pollitz, F., Wicks, C. & Thatcher, R., 2001. Mantle Flow Beneath a Continental Strike-Slip Fault: Postseismic Deformation After the 1999 Hector Mine Earthquake, *Science,* **293,** 1814–1818.

Rice, J.R. & Cleary, M.P., 1976. Some basic stress diffusion solutions for fluid-saturated elastic porous media with compressible constituents, *Rev. Geophys. Space Phys.,* **14,** 227–241.

Rodriguez, E., Morris, C.S. & Belz, J.E., 2006. A Global Assessment of the SRTM Performance. *J. Am. Soc. Photogrammetr. Remote Sens.,* **72**(3), 249–260.

Rosen, P.A., Hensley, S. & Peltzer, G., 2004. Updated Repeat Orbit Interferometry Package Released, *EOS, Trans. Am. geophys. Un.,* **85**(5), 35.

Savage, J.C., 1990. Equivalent strike-slip earthquake cycles in halfspace and lithosphere-asthenosphere Earth models. *J. geophys. Res.,* **95,** 4873–4879.

Schmidt, D.A. & Bürgmann, R., 1998. Time-dependent land uplift and subsidence in the Santa Clara valley, California, from a large interferometric synthetic aperture radar data set, *J. geophys. Res.,* **108**(B9), 2416.

Shcherbakov, R., Turcotte, D.L. & Rundle, J.B., 2004. A generalized Omori's law for earthquake aftershock decay, *Geophys. Res. Lett.,* **31,** L11613.

Unsworth, M., 2002. The Role of Crustal Fluids in Strike-slip Tectonics: New Insights from Magnetotelluric Studies. *Turkish J. earth Sci.,* **11,** 193–203.

Usai, S., 2003. A Least Squares Database Approach for SAR Interferometric Data, *IEEE Trans. Geosci. Remote Sens.,* **41**(4), 753–760.

Velasco, A.A., Ammon, C.J. & Beck, S.L., 2000. Broadband source modeling of the November 8, 1997, Tibet $M_w = 7.5$ earthquake and its tectonic implications, *J. geophys. Res.,* **105,** 28 065–28 080.

Wei, W., *et al.*, 2001. Detection of Widespread Fluids in the Tibetan Crust by Magnetotelluric Studies, *Science,* **292,** 716–718.

Wessel, P. & Smith, W.H.F., 1998. New, Improved Version of Generic Mapping Tools Released, *EOS, Trans. Am. geophys. Un.,* **79**(47), 579.

Wright, T.J., Parsons, B., England, P.C. & Fielding, E.J., 2004. InSAR Observations of Low Slip Rates on the Major Faults of Western Tibet, *Science,* **305,** 236–239.

Zhu, L. & Helmberger, D.V., 1998. Moho Offset Across the Northern Margin of the Tibetan Plateau, *Science,* **281,** 1170–1172.

Zhu, L., Zeng, R., Wu, F.T., Owens, T.J. & Randall, G., 1993. Preliminary Study of Crust-Upper Mantle Structure of the Tibetan Plateau by Using Broadband Teleseismic Body Waveforms. *Acta Seismol. Sin.,* **6, 2,** 305–316.